

An XFEM-based method with reduction technique for modeling hydraulic fracture propagation in formations containing frictional natural fractures



Fang Shi^a, Xiaolong Wang^a, Chuang Liu^a, He Liu^b, Hengan Wu^{a,*}

^a CAS Key Laboratory of Mechanical Behavior and Design of Materials, Department of Modern Mechanics, University of Science and Technology of China, Hefei, Anhui 230027, China

^b PetroChina Research Institute of Petroleum Exploration & Development, 20 Xueyuan Road, Haidian District, Beijing 100083, China

ARTICLE INFO

Article history:

Received 9 November 2016

Received in revised form 29 January 2017

Accepted 30 January 2017

Available online 9 February 2017

Keywords:

Hydraulic fracturing
XFEM
Frictional fracture
Reduction technique

ABSTRACT

Field-scale modeling of hydraulic fracture development in formations containing pre-existing fractures is a time-consuming task for XFEM-based numerical models. Because the costly solving of large-scale linear equation systems has to be performed for many times during two types of iteration processes of solving the fluid-solid coupling equations and determining the contact status between frictional fracture surfaces. In view of this challenge, a reduction technique is proposed in a tightly coupled model in which the equilibrium and flow continuity equations are solved simultaneously by the Newton-Raphson method. By retaining the enriched degrees of freedom (DOFs) and removing the standard DOFs which have no contribution to fracture opening, the dimensions of linear equation systems to be solved for both the fluid-solid coupling iteration and the nonlinear contact iteration can be significantly reduced. In the coupled model, the continuity of pressure and the mass balance at intersections of hydro-fractures are automatically achieved by sharing a common fluid node. The contact behavior of frictional fractures is modeled using the penalty method within the framework of plasticity theory of friction. Moreover, the extended Renshaw and Pollard criterion is utilized to predict whether a hydro-fracture will propagate across the frictional fracture. Simulation results indicate that the reduction technique can significantly accelerate the simulation without worsening the convergence or losing the computational accuracy for both types of iterations, and the acceleration effect becomes more remarkable as the problem scale increases. The great advantages of XFEM as well as the computational efficiency make the proposed method an attractive tool for engineering design of hydraulic fracturing treatments.

© 2017 Elsevier Ltd. All rights reserved.

1. Introduction

Hydraulic fracturing has been used in a wide range of engineering areas. As an effective stimulation strategy, it is widely applied to enhance production of conventional and unconventional oil and gas reservoirs [1]. Other applications include underground disposal of toxic wastes [2], stimulation of geothermal reservoir [3] and secure storage of CO₂ [4]. A typical hydraulic fracturing process involves using a high-pressure fluid to pressurize the wellbore until fractures emerge, which

* Corresponding author.

E-mail address: wuhah@ustc.edu.cn (H. Wu).

Nomenclature

a	vector of enriched DOF associated with Heaviside function
b	vector of enriched DOF associated with tip enrichment function
B	matrix of shape function derivatives
c	vector of enriched DOF associated with junction enrichment function
D	elastic tensor
D ^{cont}	contact tangent operator
<i>E</i>	elastic modulus
<i>F</i> _l	tip enrichment functions
F , F ^{ext}	force vectors
F _s , F _e	force vectors extracted from F
<i>H</i>	Heaviside function
H	global flux stiffness of fluid elements
J , J _R	Jacobian matrix of Newton-Raphson iteration
<i>J</i>	junction enrichment function
<i>k</i>	permeability of fracture
<i>k</i> _N , <i>k</i> _T	penalty parameters
<i>K</i> _I , <i>K</i> _{II}	mode-I and mode-II stress intensity factors
<i>K</i> _e	equivalent stress intensity factor
<i>K</i> _{IC}	fracture toughness
<i>K</i> _m	dimensionless fracture toughness
K	global stiffness matrix
K _{ss} , K _{se} , K _{es} , K _{ee}	sub-matrices extracted from K
n , n _Γ	outwards normal vectors
<i>N</i>	standard finite element shape function
<i>N</i> ^p	shape function of fluid element
N ^p , N ^u , N ^w	matrices of shape functions
<i>p</i>	fluid pressure
P	fluid pressure vector
<i>q</i>	fluid flux
<i>Q</i> _{inj}	injection rate of fluid
Q	matrix transferring fluid pressure into equivalent nodal forces
R , R _R	residual vectors of Newton-Raphson iteration
<i>s</i>	coordinate system along hydraulic fracture
<i>s</i> _{tip}	location of fracture tip
<i>S</i>	sets of nodes
S	source term in coupled equations
<i>t</i> , <i>Δt</i>	time and time increment
t , t ^{cont}	traction vectors
U , U _s , U _e	global nodal displacement
<i>w</i>	fracture width
w	fracture width vector
α	fracture propagation angle in the local fracture tip coordinate system
σ	stress tensor
ε	strain tensor
<i>ε</i> _{tol} ^w , <i>ε</i> _{tol} ^p , <i>ε</i> _{tol} ^c	convergence tolerances
<i>η</i> _p , <i>η</i> _w , <i>η</i> _c	convergence factors
<i>v</i>	Poisson's ratio
μ	fluid viscosity
μ _f	coulomb friction coefficient
Ω	two dimensional domain
Γ, Γ _{FF} , Γ _{HF} , Γ _t , Γ _u	boundaries

is followed by continuous injection of a large amount of fluid into emerged fractures to drive them to extend farther into the formation. In oil and gas fields, microseismic monitoring and other techniques have shown that pre-existing natural fractures in the formation further complicate the hydraulic fracture, forming complex fracture network [5–7]. In addition, the short- and long-term production of the reservoir is directly related to the complexity of the created fracture network which

is heavily influenced by the pre-existing natural fractures. Thus, being able to correctly predict complex hydraulic fracture development process during fracturing treatments is of great value for the stimulation design and productivity evaluation of reservoirs.

It is commonly known that theoretically clarifying the mechanism of hydraulic fracturing is particularly difficult even under considerable assumptions. From the point of view of numerical simulation, modeling of hydraulic fracturing in naturally fractured formation is also a challenging task due to a variety of physical processes involved in the problem, such as fluid flow within fractures, mechanical deformation of fractures induced by fluid pressure, propagation of fractures, interaction of hydraulic fractures and natural fractures and frictional slip along frictional natural fractures. In the last few decades, due to the efforts of many scholars, a number of numerical methods have been adopted to simulate the hydraulic fracturing process, among which the most widely used are the displacement discontinuity method (DDM) [5,8–14], the distinct element method (DEM) [15–17], the finite element method (FEM) [18–22], and the extended finite element method (XFEM) [23–31]. The DDM is developed on the basis of the boundary element method [32] and is quite suitable for modeling fractures. In the DEM, the rock mass is treated as a combination of discrete blocks connected by fractures or faults, and in consequence, the propagation paths of fractures are restricted to the edges of discrete blocks. On the other hand, the computational cost of DEM is extremely expensive when a large number of blocks are involved [33]. The FEM is a flexible, effective and widely used numerical method. However, simulation of a large number of fractures in reservoirs using FEM is very time-consuming due to the remeshing as fractures propagate. What's more, in some cases when remeshing, results need to be projected from the old mesh to the new one, which further increases the computational cost [34]. In view of these shortcomings of FEM, some improvement methods have been proposed, among which the most effective one is the XFEM.

In the XFEM, no remeshing is required during fracture propagation, and the discontinuity is modeled by introducing additional enriched degrees of freedom (DOFs) to the nodes whose support domains are cut by fractures [35–39]. This method shows great potential for modeling hydraulic fracturing due to its characteristic of mesh-independence and the convenience of handling intersections between hydro-fractures and natural fractures by introducing the junction enrichment function [26,40]. In recent years, attracted by the great advantages of XFEM, some researchers have used it to model hydraulic fracturing and fluid flow in porous media. Lecampion [23] proposed a model to investigate the solution of hydraulic fracturing problem in different propagation regimes (viscosity-dominated and toughness-dominated regimes) in non-porous formation. Dahi-Taleghani and Olson [7] used XFEM to simulate hydraulic fracture growth accounting for the effect of the natural fracture. Mohammadnejad and Khoei [24] developed a fully coupled XFEM model to simulate the hydraulically driven fracture propagation in porous media. They also [41] developed an XFEM-based model to simulate the flow of wetting and non-wetting pore fluids in progressively fracturing, partially saturated porous media. Then, Khoei et al. [42] further extended their work by employing and comparing two alternative algorithms to compute the interfacial forces due to fluid pressure exerted on the fracture faces based on a 'partitioned solution algorithm' and a 'time-dependent constant pressure algorithm'. In addition, Gordeliy and Peirce [25] proposed two different schemes for fracture with fluid lag and fracture with singular tip pressure. Dahi-Taleghani and Olson [30] studied the influence of cemented natural fractures on the hydro-fracture geometry using XFEM, but their model assumes constant pressure distribution within the fracture network. Shi et al. [31] proposed a coupled XFEM-based model for modeling hydraulic fracturing in consideration of proppant. Khoei et al. [26,29] utilized the XFEM to investigate the interaction between the hydro-fracture and the frictional natural fracture in impermeable media. Recently, Khoei et al. [43] proposed a numerical model of two-phase fluid flow in deformable porous media containing fractures with multiple length scales using XFEM and an equivalent continuum model.

Due to its significant influence on the flow of oil or gas, many numerical studies in the literature focus on the formation mechanisms of fracture network during fracturing treatments. Weng [5] presented a broad and detailed overview of existing numerical models of hydraulic fracturing designed to simulate complex fractures in naturally fractured formation. However, in the published literature, the XFEM-based model has not yet been specifically applied to large-scale simulations of hydraulic fracturing considering non-constant fluid pressure in reservoirs containing frictional natural fractures. One key issue that limits the application of XFEM to this kind of simulations is the high computational cost induced by the iteration required to solve the fluid-solid coupling (named as FSC for short) equations and the iteration required to determine the contact status between frictional fracture surfaces [26,29]. Generally, the fluid pressure distribution should be iteratively calculated by the fixed-point iteration or the Newton-Raphson iteration [44]. Besides, as the contact conditions between fractures faces are correlated to the distribution of fluid pressure inside fractures, it is necessary to detect and update contact conditions during the FSC iteration by performing the contact iteration. During each iteration (no matter the FSC iteration or the contact iteration), the dimensionality of the coupled equations to be solved is directly related to the sum of standard DOFs and additional enriched DOFs, and is usually very large for a reservoir-scale simulation. More importantly, the required CPU time to solve a linear system of equations increases rapidly as its dimensionality increases. In practice, solving a system of linear equations has a complexity of $O(n^3)$ at most, and at least n^2 operations are required to solve a system of n linear equations [45]. Therefore, the total computational cost may be considerably high for a typical reservoir-scale simulation where multiple iterations are required to be performed before achieving acceptable results. In view of the challenge outlined above, the purpose of this paper is to improve the computational efficiency in the XFEM modeling of the hydraulic processes involving frictional fractures. The reduction technique was first developed by Guyan [46] to reduce the size of the stiffness and mass matrices in the eigenvalue-eigenvector problem by eliminating elements corresponding to nodes at which no forces are applied. Since then, this technique has been widely used in linear and nonlinear dynamic response analyses [47,48], and contact problems [49]. Recently, Bao et al. [22] applied the reduction technique to the simulation of a single fracture propagation

driven by fluid pressure using finite element method without considering natural fractures. Therefore, in this study, a fully coupled hydraulic fracturing model combined with a reduction technique, which takes advantage of the fact that the fracture widths directly and exclusively depend on the degrees of freedom of enriched nodes, is proposed. The proposed model has two features: (1) the model incorporates key physical mechanisms during the development process of complex fracture network, such as interaction of hydraulic fractures and natural fractures, stress shadow effect, fluid flow within fracture network, contact conditions of fractures, and (2) the model is able to simulate the complicated physical process with high computational efficiency.

The rest of the paper is organized as follows. The mathematical description of the problem and the governing equations are given in Section 2. The reduction technique applied to both the fluid-solid coupling iteration and contact iteration is detailed in Section 3. Then, the proposed approach is verified and illustrated in Section 4. At last, conclusions are made in Section 5.

2. Problem formulation

Consider a two-dimensional domain Ω containing a hydraulically driven fracture Γ_{HF} filled with high-pressure incompressible fluid injected at a constant rate of Q_{inj} , as illustrated in Fig. 1. The domain also contains a pre-existing frictional natural fracture Γ_{FF} whose faces may undergo frictional slip in some cases as the hydraulic fracture (or named as hydro-fracture) Γ_{HF} approaches to it. The boundary of the domain is Γ and the unit outwards normal vector of Γ is represented by \mathbf{n}_Γ . The prescribed tractions \mathbf{t} and the displacements $\bar{\mathbf{u}}$ are imposed on the boundary Γ_t and Γ_u , respectively. The two faces of fractures are expressed by the positive “+” and the negative “−” signs. The unit outwards normal vectors of the negative faces of the hydro-fracture Γ_{HF} and the frictional fracture Γ_{FF} are denoted by $\mathbf{n}_{\Gamma_{HF}}$ and $\mathbf{n}_{\Gamma_{FF}}$, respectively. We define a one-dimensional curvilinear coordinate system (denoted by s) along the hydro-fracture, and the origin of the coordinate system is positioned at the injection point.

Some assumptions are made in this paper. We assume that the fluid can be typically modeled as a Newtonian fluid, the propagation of the fracture is a quasi-static process, and there is no fluid lag between the fracture tip and the fluid front. The fluid leak-off into the surrounding rock formation is neglected for simplicity since it is not the critical point in the present study. In addition, the rock formation is considered as brittle material.

2.1. Deformation and fracture propagation criterion

The strong form of the equilibrium equation of the domain in the absence of body forces can be expressed as [26]

$$\nabla \cdot \boldsymbol{\sigma} = \mathbf{0} \quad \text{in } \Omega \quad (1)$$

where $\boldsymbol{\sigma}$ is the Cauchy stress tensor, and $\nabla \cdot$ is the divergence operator. The boundary conditions can be expressed as

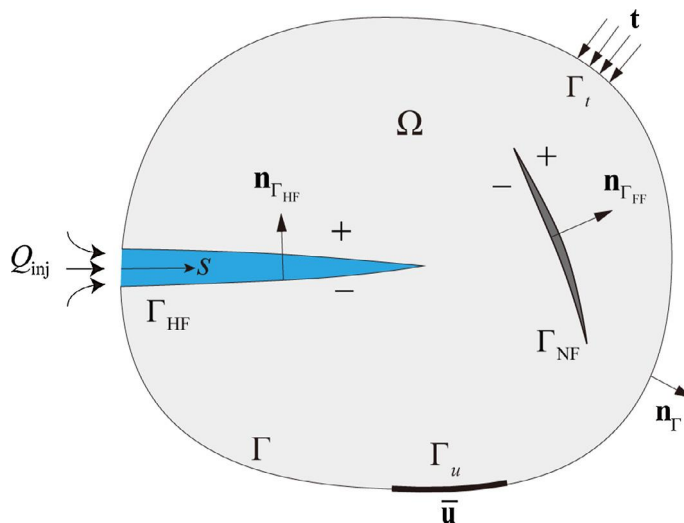


Fig. 1. Illustration of a domain containing a hydro-fracture filled with high-pressure fluid and a frictional natural fracture.

$$\begin{cases} \mathbf{u} = \bar{\mathbf{u}} & \text{on } \Gamma_u \\ \boldsymbol{\sigma} \cdot \mathbf{n} = \mathbf{t} & \text{on } \Gamma_t \\ \boldsymbol{\sigma} \cdot \mathbf{n}_{\Gamma_{HF}} = p \mathbf{n}_{\Gamma_{HF}} & \text{on } \Gamma_{HF} \\ \boldsymbol{\sigma} \cdot \mathbf{n}_{\Gamma_{FF}} = \mathbf{t}^{\text{cont}} & \text{on } \Gamma_{FF} \end{cases} \quad (2)$$

where p represents the fluid pressure, \mathbf{t}^{cont} is the contact traction vector acting on the faces of frictional fracture Γ_{FF} .

Linear elastic constitutive is applied to describe the behavior of the formation, that is

$$\boldsymbol{\sigma} = \mathbf{D} : \boldsymbol{\varepsilon} \quad (3)$$

in which \mathbf{D} is the elasticity matrix, $\boldsymbol{\varepsilon}$ is the strain tensor associated with displacement \mathbf{u} . Under the assumption of small deformation, $\boldsymbol{\varepsilon}$ can be determined from

$$\boldsymbol{\varepsilon} = \frac{1}{2} \left(\nabla \mathbf{u} + (\nabla \mathbf{u})^T \right) \quad (4)$$

The maximum hoop tensile stress criterion [50] is used to determine when and how the fracture propagates. This criterion assumes that the propagation direction is along a direction normal to the maximum hoop tensile stress, and when the equivalent stress intensity factor K_e is greater than or equal to the fracture toughness of the rock formation, K_{IC} , the fracture will propagate. In this paper, the domain forms of the interaction integral method [51] are used to determine the stress intensity factors K_I and K_{II} . The equivalent stress intensity factor K_e is calculated as [50]

$$K_e = \cos \frac{\alpha}{2} \left(K_I \cos^2 \frac{\alpha}{2} - \frac{3K_{II}}{2} \sin \alpha \right) \quad (5)$$

where α is the fracture propagation angle in the local fracture tip coordinate system and can be determined by

$$\alpha = 2 \arctan \left(\frac{-2K_{II}/K_I}{1 + \sqrt{1 + 8(K_{II}/K_I)^2}} \right) \quad (6)$$

2.2. Fluid flow

The one-dimensional flow of fluid in the hydro-fracture must satisfy the mass conservation equation. For any point s along the hydro-fracture, this equation can be expressed as [44]

$$\frac{\partial w}{\partial t} + \frac{\partial q}{\partial s} = 0 \quad (7)$$

where w represents the width of the hydro-fracture; q is the fluid flux. Under the lubrication theory, fluid flux within the hydro-fracture can be given according to Poiseuille's law [52]

$$q = -\frac{w^3}{12\mu} \frac{\partial p}{\partial s} \quad (8)$$

where μ represents the viscosity of the fluid. Substituting Eq. (8) into Eq. (7) leads to the following equation [22]

$$\frac{\partial w}{\partial t} - \frac{\partial}{\partial s} \left(k \frac{\partial p}{\partial s} \right) = 0 \quad (9)$$

where k can be considered as the permeability of the hydro-fracture and

$$k = \frac{w^3}{12\mu} \quad (10)$$

For a hydro-fracture, Eq. (9) can be solved with the following initial and boundary conditions

$$\begin{cases} w(s, 0) = 0 \\ w(s_{tip}, t) = 0 \\ q(0, t) = Q_{\text{inj}} \\ q(s_{tip}, t) = 0 \end{cases} \quad (11)$$

as well as the global mass conservation equation

$$\int_0^{s_{tip}} w ds = \int_0^t Q_{\text{inj}} dt \quad (12)$$

where s_{tip} represents the location of the hydro-fracture tip and Q_{inj} represents the injection rate of fluid at the injection point.

For a T-shaped fluid-driven fracture formed after the intersection of a hydraulic fracture and a natural fracture, as shown in Fig. 2, the same fluid pressure should be imposed at the junction for all branches. In addition, the balance of flux into and out of the junction should also be imposed due to the law of conservation of mass [8,12]. In this paper, the continuity of pressure and mass balance at the junction can be automatically satisfied in the proposed coupling method by sharing a common fluid node, as will be shown later in Section 2.4.

2.3. Weak form of governing equations

By introducing the trial function $\mathbf{u}(\mathbf{x}, t)$ and test function $\delta\mathbf{u}(\mathbf{x}, t)$ for the displacement field, the weak form of equilibrium equation can be written as

$$\int_{\Omega} \delta\mathbf{e} : \boldsymbol{\sigma} d\Omega + \int_{\Gamma_{HF}} [[\delta\mathbf{u}]] \cdot p\mathbf{n}_{\Gamma_{HF}} d\Gamma + \int_{\Gamma_{FF}} [[\delta\mathbf{u}]] \cdot \mathbf{t}^{\text{cont}} d\Gamma = \int_{\Gamma_t} \delta\mathbf{u} \cdot \mathbf{t} d\Gamma \quad (13)$$

where the symbol $[[*]] = *^+ - *^-$ represents the difference of the variable “*” between face “+” and face “−” of fractures. Therefore, $[[\mathbf{u}]]$ stands for the displacement jump across the faces of fractures.

By introducing test function $\delta p(s, t)$ and integrating by parts, the weak form of the fluid flow equation (Eq. (9)) can be given as

$$\int_{\Gamma_{HF}} \left(\delta p \frac{\partial W}{\partial t} + \frac{\partial(\delta p)}{\partial s} k \frac{\partial p}{\partial s} \right) d\Gamma + \delta p|_{s=0} Q_{\text{inj}} = 0 \quad (14)$$

Notice that since the permeability k is related to the width of the hydro-fracture with a cubic relationship, as given in Eq. (10), the coupled equilibrium and fluid flow equations are highly nonlinear. In the current study, this nonlinear coupled system is solved simultaneously through the Newton-Raphson iterative method, as will be shown in detail in Section 3.1.

2.4. Discretization of governing equations

To discrete the equilibrium equation, the XFEM is employed to approximate the displacement field \mathbf{u} . For the hydraulic fracturing problem, the displacement \mathbf{u} for any point \mathbf{x} in the domain Ω can be approximated by adding three types of enrichment shape functions as

$$\begin{aligned} \mathbf{u}(\mathbf{x}) = & \sum_{I \in S_{\text{all}}} N_I^u(\mathbf{x}) \mathbf{u}_I + \sum_{I \in S_{\text{frac}}} N_I^u(\mathbf{x}) H(\mathbf{x}) \mathbf{a}_I \\ & + \sum_{I \in S_{\text{tip}}} N_I^u(\mathbf{x}) \sum_{l=1}^4 F_l(\mathbf{x}) \mathbf{b}_I^l + \sum_{I \in S_{\text{junction}}} N_I^u(\mathbf{x}) J(\mathbf{x}) \mathbf{c}_I \end{aligned} \quad (15)$$

where S_{all} is the set of all nodes in the mesh, S_{frac} is the set of nodes whose support domains are cut into two parts by the fracture, S_{tip} is the set of nodes whose support domains are partially cut by the fracture, and S_{junction} is the set of nodes whose support domains are split into three parts by two intersecting fractures. N_I^u is the standard finite element shape functions of

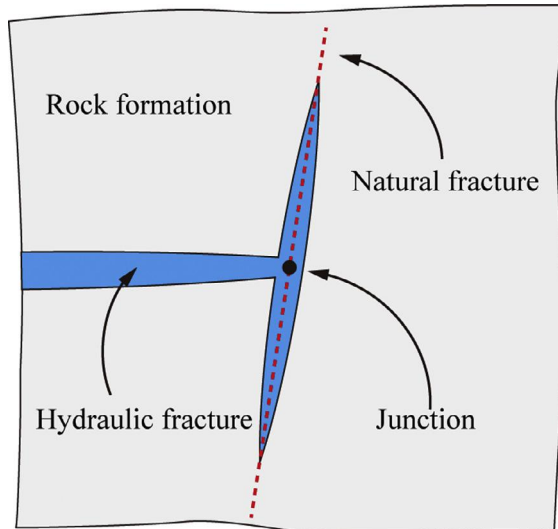


Fig. 2. Schematic of a T-shaped fluid-driven fracture formed after the intersection of a hydraulic fracture and a natural fracture.

node I . \mathbf{u}_I is the standard nodal displacement vector. \mathbf{a}_l , \mathbf{b}_l^l ($l = 1, 4$) and \mathbf{c}_l are the nodal enriched DOF vectors. $H(\mathbf{x})$, $F_l(\mathbf{x})$ and $J(\mathbf{x})$ are the enrichment shape functions to account for the displacement jump across fracture surfaces, the singular displacement field around the fracture tip and the displacement field around the intersection point of two fractures, respectively. $H(\mathbf{x})$ is usually taken as the signed Heaviside function [38]; $F_l(\mathbf{x})$ for tip enrichment in brittle materials takes the general form

$$\{F_l(r, \theta)\}_{l=1}^4 = \left\{ \sqrt{r} \sin \frac{\theta}{2}, \sqrt{r} \cos \frac{\theta}{2}, \sqrt{r} \sin \theta \sin \frac{\theta}{2}, \sqrt{r} \sin \theta \cos \frac{\theta}{2} \right\} \quad (16)$$

where (r, θ) defines the polar coordinate system with the origin at the fracture tip; $J(\mathbf{x})$ is the junction enrichment function [26]. Typically, for a T-shaped junction, J equals 1, -1 or 0 on different subdomains created by the intersected fractures. Details of the above enrichment functions can be found in the cited papers [26,37,40]. A schematic view of a typical enrichment strategy of two intersecting fractures is illustrated in Fig. 3.

To approximate the one-dimensional pressure field $p(s, t)$ inside a hydro-fracture, the fracture interface Γ_{HF} is discretized into fluid elements using linear shape functions. The nodes of the fluid elements are regularly arranged at the intersections of hydro-fractures and edges of solid elements, as well as the fracture tips, as illustrated in Fig. 3. Additionally, a common fluid node is imposed at the intersection point of two hydro-fractures and shared by all fracture branches to satisfy the continuity of pressure and the balance of mass at the intersection point. The finite element approximation of the pressure field can be expressed as

$$\mathbf{p}(s) = \sum_{I \in S_{hf}} N_I^p(s) p_I \quad (17)$$

where S_{hf} is the set of nodes of the fluid elements defined along the hydraulic fracture; $N_I^p(s)$ represents the linear shape function of nodal pressure p_I for node I , and it is defined in the natural local coordinate system ξ , namely

$$\begin{cases} N_1^p(\xi) = (\xi - 1)/2 \\ N_2^p(\xi) = (\xi + 1)/2 \end{cases} \quad (18)$$

The fracture opening displacement vector \mathbf{w} can be approximated by

$$\mathbf{w} = \sum_{I \in S_w} N_I^w \mathbf{u}_I \equiv \mathbf{N}^w \mathbf{U} \quad (19)$$

where S_w represents the set of nodes of elements that contain the fluid nodes; \mathbf{N}^w is the shape function matrix which transfers the nodal displacement to fracture opening; \mathbf{U} is the global nodal displacement vector which contains both the standard DOFs and enriched DOFs.

By substituting the displacement and pressure approximations (Eqs. (15), (17) and (19)) and the linear elastic constitutive equation (Eq. (3)) into the weak form of the equilibrium equation (Eq. (13)) and the fluid flow equation (Eq. (14)), it is straight-forward to obtain the discretized system of the nonlinear coupled equilibrium and flow continuity equations as

$$\mathbf{K}\mathbf{U} - \mathbf{Q}\mathbf{P} - \mathbf{F}^{ext} = \mathbf{0} \quad (20)$$

$$\mathbf{Q}^T \dot{\mathbf{U}} + \mathbf{H}\mathbf{P} + \mathbf{S} = \mathbf{0} \quad (21)$$

In Eq. (20), \mathbf{K} is the global stiffness matrix; the coupling matrix \mathbf{Q} that transfers fluid pressure vector \mathbf{P} into equivalent nodal forces, and the external loading vector \mathbf{F}^{ext} are defined as

$$\mathbf{Q} = \int_{\Gamma_{HF}} (\mathbf{N}^w)^T \mathbf{n}_{\Gamma_{HF}} \mathbf{N}^p d\Gamma \quad (22)$$

$$\mathbf{F}^{ext} = \int_{\Gamma_t} (\mathbf{N}^u)^T \mathbf{t} d\Gamma \quad (23)$$

In Eq. (21), the flow matrix \mathbf{H} and the source term \mathbf{S} are defined as

$$\mathbf{H} = \int_{\Gamma_{HF}} k \left(\frac{\partial \mathbf{N}^p}{\partial s} \right)^T \frac{\partial \mathbf{N}^p}{\partial s} ds \quad (24)$$

$$\mathbf{S} = \mathbf{N}^p(s)|_{s=0} Q_{inj} \quad (25)$$

Taking time integration of Eq. (21) over a time step, we can obtain

$$\int_{t_n}^{t_{n+1}} (\mathbf{Q}^T \dot{\mathbf{U}} + \mathbf{H}\mathbf{P} + \mathbf{S}) dt = \mathbf{0} \quad (26)$$

where n represents the time step number. Implicit backward Euler time discretization is used in this paper, so according to Eq. (26), we have

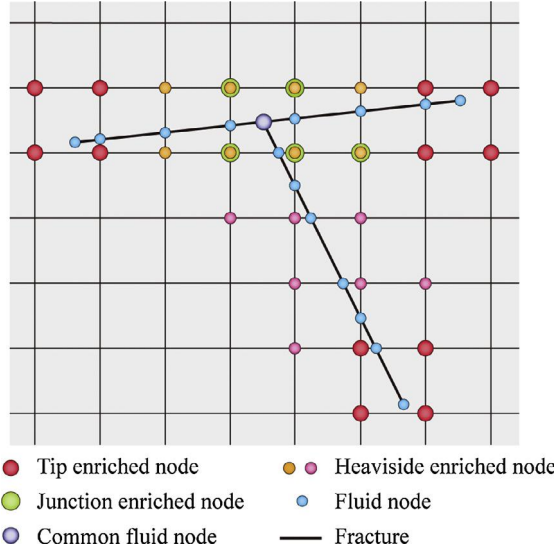


Fig. 3. Schematic of enriched nodes and fluid nodes of two intersecting hydro-fractures (T-shaped junction).

$$\mathbf{Q}^T(\mathbf{U}_{n+1} - \mathbf{U}_n) + \Delta t \mathbf{H} \mathbf{P}_{n+1} + \Delta t \mathbf{S} = \mathbf{0} \quad (27)$$

where \mathbf{U}_{n+1} , \mathbf{P}_{n+1} are the unknown displacement field and fluid pressure at the $(n+1)$ th time step, respectively; \mathbf{U}_n is the already known displacement field at the previous time step; Δt is the time increment between two adjacent time steps. In addition, after the time discretization, Eq. (20) can be rewritten as follows in every time step

$$\mathbf{K}_{n+1} \mathbf{U}_{n+1} - \mathbf{Q} \mathbf{P}_{n+1} - \mathbf{F}^{\text{ext}} = \mathbf{0} \quad (28)$$

Therefore, \mathbf{U}_{n+1} , \mathbf{P}_{n+1} can be calculated by solving the coupled Eqs. (27) and (28).

3. The reduction technique

Before continuing, it is necessary to recapitulate the general numerical solution procedure for a typical hydraulic fracturing problem in consideration of the frictional fractures. As mentioned in the introduction, there are two types of iterations to be performed during each time step: the iteration to check and determine the contact status of fractures (i.e., the contact iteration), and the iteration to solve the coupling between fluid flow and deformation of fractures (i.e., the FSC iteration). In the present work, the contact iteration is performed using the Newton-Raphson iteration method and the FSC iteration is performed using a stabilized Newton-Raphson procedure (see Appendix A for details). At the beginning of each time step, Eq. (28) is iteratively solved to determine the contact status of fractures with a pressure distribution \mathbf{P} which is given as an initial condition or obtained from the previous time step. Once the contact iteration converges, an FSC iteration step starts to solve the coupled Eqs. (27) and (28) for \mathbf{U} and \mathbf{P} with an updated contact traction vector and the associated contact stiffness matrix. Then, after the FSC iteration step, the contact solution is renewed by performing the contact iteration, which is followed by another FSC iteration step. This process continues until the FSC iteration convergence criterion is reached. It is important to mention that for the cases where the fractures intervals are wide or the fracture interactions are weak, the contact iterations need only to be performed during the first few FSC iteration steps. This will be shown in detail in Sections 4.3 and 4.4.

From the solution procedure discussed above, it can be observed that the computational cost appears to be a key problem because, usually, multiple iterations are required to obtain satisfactory convergence. Meanwhile, each iteration step means a costly solving of a large-scale linear equation system. In this section, the reduction technique is proposed as an efficient tool to reduce the total calculation time within the framework of XFEM. According to the formulation of XFEM, the displacement vector \mathbf{U} can be conveniently divided into two parts: one part is \mathbf{U}_s , which contains all the standard DOFs and has no contribution to the calculation of fracture widths; the other part \mathbf{U}_e contains all the enriched DOFs from which the fracture widths can be directly derived [23]. Similarly, the global stiffness matrix \mathbf{K} can be divided into four parts as follows

$$\begin{aligned} \mathbf{K} &= \begin{bmatrix} \int_{\Omega} (\mathbf{B}^{\text{std}})^T \mathbf{D} \mathbf{B}^{\text{std}} d\Omega & \int_{\Omega} (\mathbf{B}^{\text{std}})^T \mathbf{D} \mathbf{B}^{\text{enr}} d\Omega \\ \int_{\Omega} (\mathbf{B}^{\text{enr}})^T \mathbf{D} \mathbf{B}^{\text{std}} d\Omega & \int_{\Omega} (\mathbf{B}^{\text{enr}})^T \mathbf{D} \mathbf{B}^{\text{enr}} d\Omega + \int_{\Gamma_{\text{FF}}} (\mathbf{N}^w)^T \mathbf{D}^{\text{cont}} \mathbf{N}^w d\Gamma \end{bmatrix} \\ &\equiv \begin{bmatrix} \mathbf{K}_{ss} & \mathbf{K}_{se} \\ \mathbf{K}_{es} & \mathbf{K}_{ee} + \mathbf{K}_{ee}^{\text{cont}} \end{bmatrix} = \begin{bmatrix} \mathbf{K}_{ss} & \mathbf{K}_{se} \\ \mathbf{K}_{es} & \tilde{\mathbf{K}}_{ee} \end{bmatrix} \end{aligned} \quad (29)$$

where \mathbf{D}^{cont} is the contact tangent operator of the contact problem within the framework of plasticity theory of frictional [26,53] and is defined as

$$\mathbf{D}^{\text{cont}} = \begin{cases} k_N(\mathbf{n}_{\Gamma_{\text{FF}}} \otimes \mathbf{n}_{\Gamma_{\text{FF}}}) + k_T(\mathbf{m}_{\Gamma_{\text{FF}}} \otimes \mathbf{m}_{\Gamma_{\text{FF}}}) & \text{for stick} \\ k_N(\mathbf{n}_{\Gamma_{\text{FF}}} \otimes \mathbf{n}_{\Gamma_{\text{FF}}}) + \mu_f k_T(\mathbf{m}_{\Gamma_{\text{FF}}} \otimes \mathbf{n}_{\Gamma_{\text{FF}}}) & \text{for slip} \end{cases} \quad (30)$$

where k_N and k_T are the penalty parameters in the normal and tangential directions, respectively; μ_f is the Coulomb friction coefficient, and $\mathbf{m}_{\Gamma_{\text{FF}}}$ is the unit vector in the tangential direction of the frictional fracture.

After the decomposition of \mathbf{U} and \mathbf{K} along with the decomposition of the external force vector \mathbf{F}^{ext} into $\mathbf{F}^{\text{ext}}_s$ and $\mathbf{F}^{\text{ext}}_e$, Eq. (28) can be rewritten as

$$\begin{bmatrix} \mathbf{K}_{ss} & \mathbf{K}_{se} & \mathbf{0} \\ \mathbf{K}_{es} & \tilde{\mathbf{K}}_{ee} & -\mathbf{Q}_e \end{bmatrix} \begin{pmatrix} \mathbf{U}_s \\ \mathbf{U}_e \\ \mathbf{P} \end{pmatrix} - \begin{pmatrix} \mathbf{F}^{\text{ext}}_s \\ \mathbf{F}^{\text{ext}}_e \\ \mathbf{0} \end{pmatrix} = \mathbf{0} \quad (31)$$

in which \mathbf{Q}_e is a sub-matrix extracted from matrix \mathbf{Q} by deleting terms related to standard DOFs. The subscripts n in Eq. (28), which represent the time step, are omitted for brevity's sake. It is obvious that $\mathbf{F}^{\text{ext}}_e$ is zero vectors since there are no external forces acting on the enriched DOFs. Thus, Eq. (31) can be further written as

$$\begin{bmatrix} \mathbf{K}_{ss} & \mathbf{K}_{se} & \mathbf{0} \\ \mathbf{K}_{es} & \tilde{\mathbf{K}}_{ee} & -\mathbf{Q}_e \end{bmatrix} \begin{pmatrix} \mathbf{U}_s \\ \mathbf{U}_e \\ \mathbf{P} \end{pmatrix} - \begin{pmatrix} \mathbf{F}^{\text{ext}}_s \\ \mathbf{0} \\ \mathbf{0} \end{pmatrix} = \mathbf{0} \quad (32)$$

Then Eq. (32) can be equivalently expressed as two equations

$$\mathbf{K}_{ss}\mathbf{U}_s + \mathbf{K}_{se}\mathbf{U}_e - \mathbf{F}^{\text{ext}}_s = \mathbf{0} \quad (33)$$

$$\mathbf{K}_{es}\mathbf{U}_s + \tilde{\mathbf{K}}_{ee}\mathbf{U}_e - \mathbf{Q}_e\mathbf{P} = \mathbf{0} \quad (34)$$

Substituting the rearranged Eq. (33) in which \mathbf{U}_s is explicitly expressed into Eq. (34) yields the following equation

$$(\tilde{\mathbf{K}}_{ee} - \mathbf{K}_{es}\mathbf{K}_{ss}^{-1}\mathbf{K}_{se})\mathbf{U}_e + \mathbf{K}_{es}\mathbf{K}_{ss}^{-1}\mathbf{F}^{\text{ext}}_s - \mathbf{Q}_e\mathbf{P} = \mathbf{0} \quad (35)$$

So far, with the above reduction operation, the original discretized equilibrium equation (Eq. (28)) has been replaced with the dimension-reduced equation (Eq. (35)).

3.1. Application to fluid-solid coupling iteration

To make the presentation clear, we start with the Newton-Raphson procedure for the fluid-solid coupling problem without applying the reduction technique. For coupled Eqs. (27) and (28), the residual vector \mathbf{R}^i of the Newton-Raphson method at the iteration step i can be expressed as

$$\mathbf{R}^i = \begin{bmatrix} \mathbf{0} & \mathbf{0} \\ -\mathbf{Q}^T & \mathbf{0} \end{bmatrix} \begin{pmatrix} \Delta\mathbf{U} \\ \Delta\mathbf{P} \end{pmatrix}^i + \begin{bmatrix} \mathbf{K} & -\mathbf{Q} \\ \mathbf{0} & -\Delta t\mathbf{H}^i \end{bmatrix} \begin{pmatrix} \mathbf{U} \\ \mathbf{P} \end{pmatrix}^i - \begin{pmatrix} \mathbf{F}^{\text{ext}} \\ \Delta t\mathbf{S}^i \end{pmatrix}^i \quad (36)$$

and the Jacobian matrix of the residual \mathbf{R}^i can be written as

$$\mathbf{J}^i = \begin{bmatrix} \mathbf{K} & -\mathbf{Q} \\ -\mathbf{Q}^T & -\Delta t\mathbf{H}^i \end{bmatrix} \quad (37)$$

Then the displacement \mathbf{U} and fluid pressure \mathbf{P} can be updated according to

$$\begin{pmatrix} \mathbf{U} \\ \mathbf{P} \end{pmatrix}^{i+1} = \begin{pmatrix} \mathbf{U} \\ \mathbf{P} \end{pmatrix}^i - \frac{\mathbf{R}^i}{\mathbf{J}^i} \quad (38)$$

For the reduced coupled Eqs. (27) and (35), the residual vector \mathbf{R}_R^i (the subscript R stands for “Reduce”, similarly hereinafter) of the Newton-Raphson method at the iteration step i can be expressed as

$$\mathbf{R}_R^i = \begin{bmatrix} \mathbf{0} & \mathbf{0} \\ -\mathbf{Q}_e^T & \mathbf{0} \end{bmatrix} \begin{pmatrix} \Delta\mathbf{U}_e \\ \Delta\mathbf{P} \end{pmatrix}^i + \begin{bmatrix} \tilde{\mathbf{K}}_{ee} - \mathbf{K}_{es}\mathbf{K}_{ss}^{-1}\mathbf{K}_{se} & -\mathbf{Q}_e \\ \mathbf{0} & -\Delta t\mathbf{H}^i \end{bmatrix} \begin{pmatrix} \mathbf{U}_e \\ \mathbf{P} \end{pmatrix}^i - \begin{pmatrix} -\mathbf{K}_{es}\mathbf{K}_{ss}^{-1}\mathbf{F}^{\text{ext}}_s \\ \Delta t\mathbf{S}^i \end{pmatrix}^i \quad (39)$$

The Jacobian matrix of the residual \mathbf{R}_R^i can be written as

$$\mathbf{J}_R^i = \begin{bmatrix} \tilde{\mathbf{K}}_{ee} - \mathbf{K}_{es}\mathbf{K}_{ss}^{-1}\mathbf{K}_{se} & -\mathbf{Q}_e \\ -\mathbf{Q}_e^T & -\Delta t\mathbf{H}^i \end{bmatrix} \quad (40)$$

Then the displacement \mathbf{U}_e related to the enriched DOFs and fluid pressure \mathbf{P} can be updated by

$$\begin{pmatrix} \mathbf{U}_e \\ \mathbf{P} \end{pmatrix}^{i+1} = \begin{pmatrix} \mathbf{U}_e \\ \mathbf{P} \end{pmatrix}^i - \frac{\mathbf{R}_R^i}{\mathbf{J}_R^i} \quad (41)$$

The iteration converges when fracture width \mathbf{w} and fluid pressure \mathbf{P} both come to a steady state, i.e., when the following two criteria are satisfied simultaneously

$$\begin{cases} \eta_p = \|\mathbf{P}^{i+1} - \mathbf{P}^i\| / \|\mathbf{P}^i\| \leq \varepsilon_{tol}^p \\ \eta_w = \|\mathbf{w}^{i+1} - \mathbf{w}^i\| / \|\mathbf{w}^i\| \leq \varepsilon_{tol}^w \end{cases} \quad (42)$$

where $\|\cdot\|$ represents the L2-norm operator; ε_{tol}^w and ε_{tol}^p are the specified tolerances and are both taken as 10^{-4} in this paper.

It should be noted that when trying to calculate \mathbf{R}_R^i and \mathbf{J}_R^i in Eqs. (39) and (40), the inverse matrix, \mathbf{K}_{ss}^{-1} , which is, in general, a dense matrix rather than a sparse matrix should be obtained first, and this procedure requires a relatively high computational cost. Fortunately, the matrix inversion of \mathbf{K}_{ss} needs to be performed only once at the beginning of the analysis, as \mathbf{K}_{ss} remains unchanged throughout the analysis. Once the Newton-Raphson iteration converges, \mathbf{U}_s can then be easily obtained according to Eq. (33) as \mathbf{K}_{ss}^{-1} is already known. In general, the number of the enriched DOFs is quite less than the number of the standard DOFs for a hydraulic fracturing simulation. Therefore, the computational cost can be dramatically reduced by using the reduction technique. Moreover, in the case of the reduced equilibrium equation, the structural complexity remains the same because all elements of the original stiffness matrix contribute. Hence, theoretically speaking, the proposed reduction technique has no effect on iteration performance and simulation results as will be shown in Section 4.

3.2. Application to contact iteration

In general, there are two types of natural fractures in the formation: cemented fractures [54] and frictional fractures. Unlike the cemented fractures, the contact status of each frictional natural fracture must be determined. For a typical contact problem, a variety of techniques can be used to incorporate the contact constraints into the weak form of XFEM equilibrium equation, among which the most frequently used are the penalty method [26,53,55], the augmented-Lagrange multipliers method [56] and the Lagrange multipliers method [57]. Since it introduces no additional variables, the penalty method is widely used. Consequently, the penalty method in the framework of frictional plasticity theory [26,53] is used to illustrate the reduction technique in this paper. Yet, it is worth stating that the proposed reduction technique is independent of the contact algorithm.

When considering the frictional interaction between fracture surfaces, the discretized reduced equilibrium equation (Eq. (35)) is not linear because $\tilde{\mathbf{K}}_{ee}$ consists of a contact stiffness matrix $\mathbf{K}_{ee}^{\text{cont}}$ that incorporates the unknown contact condition related to displacement \mathbf{U} into the XFEM formulation, as given in Eq. (29). Therefore, Eq. (35) should be iteratively solved to predict the stick/slip condition along fractures. The predictor-corrector algorithm similar to the elastic-predictor/plastic-corrector algorithm in the classical plastic theory [58] is adopted to obtain the contact tractions and update the penalty parameters for the frictional contact problem. The detailed description of the Kuhn-Tucker rules expressing contact conditions, the Coulomb's friction law for the description of frictional contact behavior, as well as the predictor-corrector algorithm can be found in the cited papers [26,53], and will not be repeated here as they are not the main concern of the present work.

For the reduced equilibrium equation (Eq. (35)), the residual vector $\hat{\mathbf{R}}_R^i$ of the Newton-Raphson method at the contact iteration step i can be written as

$$\hat{\mathbf{R}}_R^i = (\tilde{\mathbf{K}}_{ee}^i - \mathbf{K}_{es}\mathbf{K}_{ss}^{-1}\mathbf{K}_{se})\mathbf{U}_e^i - \mathbf{Q}_e\mathbf{P} + \mathbf{K}_{es}\mathbf{K}_{ss}^{-1}\mathbf{F}_s^{\text{ext}} \quad (43)$$

and the associated Jacobian matrix can be written as

$$\hat{\mathbf{J}}_R^i = \tilde{\mathbf{K}}_{ee}^i - \mathbf{K}_{es}\mathbf{K}_{ss}^{-1}\mathbf{K}_{se} \quad (44)$$

Thus \mathbf{U}_e can be updated at each iteration by

$$\mathbf{U}_e^{i+1} = \mathbf{U}_e^i - \frac{\hat{\mathbf{R}}_R^i}{\hat{\mathbf{J}}_R^i} \quad (45)$$

The contact iteration converges when the residual vector $\hat{\mathbf{R}}_R^i$ is small enough in comparison with the initial residual vector $\hat{\mathbf{R}}_R^0$

$$\eta_c = \|\hat{\mathbf{R}}_R^i\| / \|\hat{\mathbf{R}}_R^0\| \leq \varepsilon_{tol}^c \quad (46)$$

where the tolerance ε_{tol}^c is taken as 10^{-10} in this paper.

4. Numerical examples

In order to verify the accuracy and demonstrate the performance of the proposed approach, four numerical examples are presented in this section. For these simulations, one-dimensional Gauss integration scheme with two integration points [57] is used to perform the numerical integration over both the fluid elements and the contact faces along fracture segments. In addition, a dynamic time step Δt [22] is used to ensure the mass conservation equation (Eq. (20)). The in-house program (<http://phipsi.top>) used in this paper is written in FORTRAN 90. A numerical library called LAPACK [59] has been integrated into the program to solve the linear systems of equations. Additionally, a backtracking algorithm is introduced to improve the robustness of the Newton-Raphson method for the FSC iteration (details of the stabilized Newton-Raphson method can be found in Appendix A). All simulations are performed on a computer with Intel i7-4790K 4 GHz processor and 16 GB DDR3 memory.

4.1. Verification of reduction technique for fluid-solid coupling iteration

As a starting point, we verify the reduction technique for the fluid-solid coupling iteration without considering contact by comparing the numerical results with analytical solutions [60]. The analytical solutions have different expressions depending on the dimensionless fracture toughness K_m of the KGD model [61] which can be written as

$$K_m = 4 \left(\frac{2}{\pi} \right)^{1/2} \frac{K_{IC}(1 - v^2)}{E} \left[\frac{E}{12\mu Q_{inj}(1 - v^2)} \right]^{1/4} \quad (47)$$

where E and v are the elastic modulus and the Poisson's ratio of the rock formation, respectively. The fracture propagation regime is viscosity-dominated when $K_m < 1$ and toughness-dominated when $K_m > 4$. Since the fluid pressure along the hydro-fracture is nearly constant, treatments in the toughness-dominated regime, such as slickwater fracturing, are relatively easy to be modeled and convergence can be achieved in a few iterations at each time step without consuming too much CPU time [22]. In addition, the viscosity-dominated regime is much more common for industrial hydraulic fracturing [62]. Therefore, treatments in the toughness-dominated regime are not discussed in this paper. Nevertheless, it should be noted that the reduction technique is also applicable to toughness-dominated cases without any additional consideration.

In this verification, the hydro-fracture is positioned at the center of a symmetrical model which has dimensions of 100 m and 180 m in x and y directions, respectively, as shown in Fig. 4. The left edge of the model is fixed in x direction and the bottom-left corner is fixed in both x and y directions. The material properties and fracturing parameters are listed in Table 1. The fracture propagation regime is viscosity-dominated as K_m is equal to 0.0313 and is much smaller than 1. The finite element mesh of the model which contains 3080 four-node quadrilateral elements is also shown in Fig. 4. The size of elements around the hydro-fracture is 0.5 m \times 0.5 m.

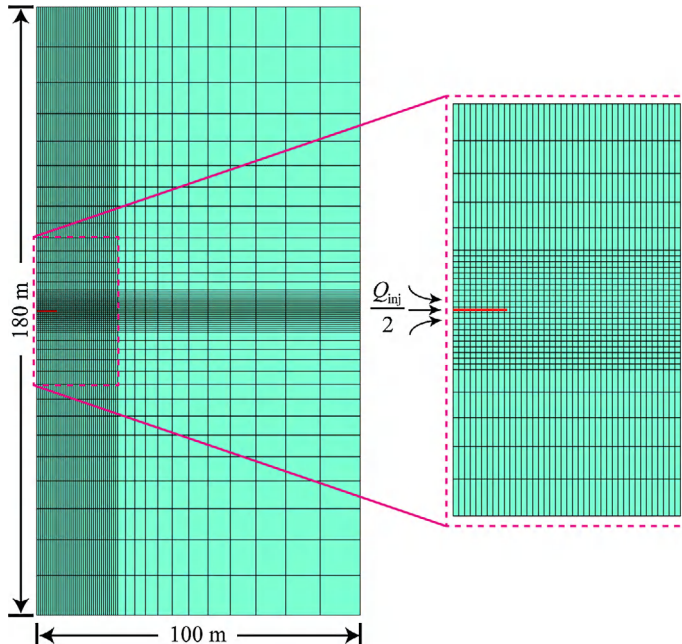


Fig. 4. Geometry and finite element mesh of symmetrical hydraulic fracture propagation model.

Table 1
Material properties and fracturing parameters.

Parameter	Units	Value
Elastic modulus E	GPa	20
Poisson's ratio ν	–	0.2
Fracture toughness K_{IC}	MPa m ^{1/2}	0.1
Injection rate Q_{inj}	m ² /s	0.001
Viscosity μ	Pa s	0.1
Dimensionless toughness K_m	–	0.0313

The initial half-length of the hydro-fracture is 1.25 m. A uniform pressure of 3.9 MPa, which is the theoretical fluid pressure at the injection point, is taken as the initial guess for the first time step of the Newton-Raphson iteration. For the subsequent time steps, the pressure solution obtained from the previous step is chosen as the first estimate. The simulation continues until the injection time reaches 30 s. The variations of fluid pressure at the injection point and the fracture width profiles at 30 s are shown in Figs. 5 and 6, respectively, together with the corresponding analytical solutions for comparison. Excellent agreement between the numerical results and analytical solutions can be found, indicating that the proposed approaches with and without the reduction technique are both able to predict satisfactory results. In addition, the complete overlap of numerical results with and without the reduction technique shows that the reduction technique has no effect on simulation results, as mentioned at the end of Section 3.1.

To illustrate the performance of the reduction technique, the acceleration ratio is defined as the ratio of the total CPU times consumed by the simulation without the reduction technique to that with the reduction technique. The evolution of CPU times and corresponding acceleration ratio are shown in Fig. 7, in which the acceleration ratio gradually increases from 0.9 to 5.2, indicating a remarkable reduction of computational cost when the reduction technique is applied. Indeed, this significant improvement is attributed to the remarkable decrease of the dimensions of linear systems to be solved at each time step, with values ranging from 6370 to 6460, and from 43 to 133, for schemes without and with the reduction technique, respectively. What calls for special attention is that the minimum value of the acceleration ratio, which is equal to 0.9 and less than 1, occurs at the first time step where a relatively time-consuming inverse operation of \mathbf{K}_{ss} needs to be performed. Furthermore, another fact should be pointed out about the acceleration ratio. The total consumed CPU time consists of two main components: component (1) time required to solve the linear systems of equations; and component (2) time required by other numerical operations such as determination of enriched nodes, assembly of matrices, calculation of stress intensity factors, data transfer, preparation of data for post-process analyses, and so on. However, the computational cost incurred by solving systems of linear algebraic equations is, in general, the dominated cost for a typical FEM-based analysis [34], and rapidly overwhelms other computational phases when the scale of analysis is increased. Thus, for reasons that have been given above and will be clarified in the following, it is of great importance to adopt the reduction technique in an XFEM-based hydraulic fracturing simulation.

The number of Newton-Raphson iterations required to solve the coupling equations with the convergence tolerance of 10^{-4} is shown in Fig. 8, from which we can see that, as expected, the reduction technique has no effect on the number of

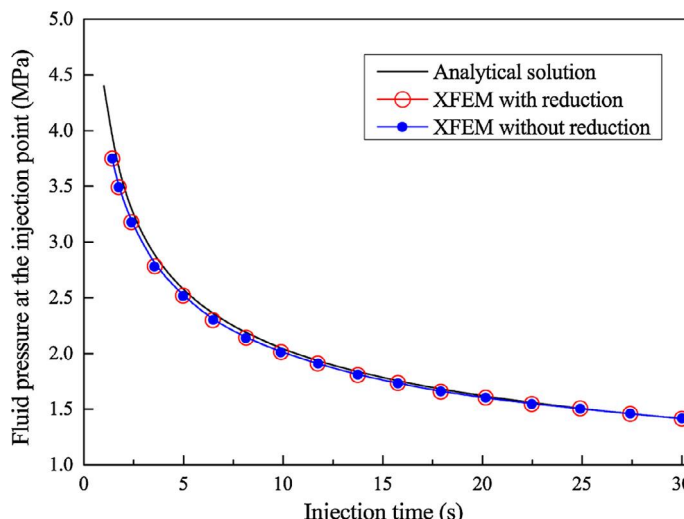


Fig. 5. Comparison of fluid pressures at the injection point from XFEM and analytical solution at various instants.

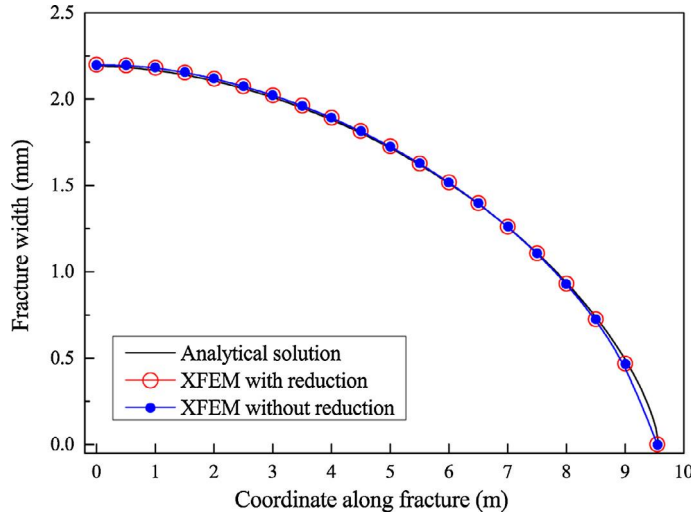


Fig. 6. Comparison of fracture widths from XFEM and analytical solution when injection time reaches 30 s.

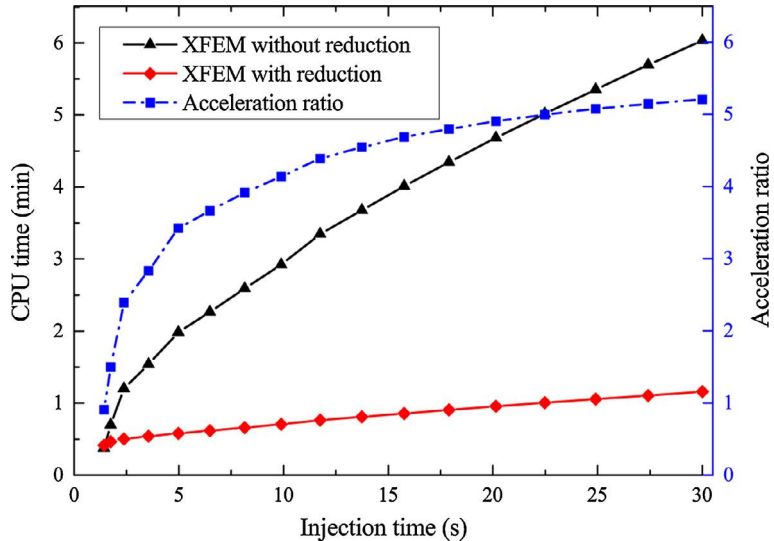


Fig. 7. Consumed CPU times and acceleration ratio at different injection times of verification example of hydraulic fracturing.

iterations. Finally, Fig. 9 demonstrates the performance of convergence at the last time step, and a similar conclusion can be drawn due to the overlap of the convergence curves.

4.2. Verification of reduction technique for contact iteration

In this section, the reduction technique for the contact problem is evaluated through a uniaxial compression simulation of a plane strain block, which centrally contains an oblique frictional fracture at the angle of 50 degrees relative to the horizontal direction. The block has dimensions of 35 m × 50 m, as shown in Fig. 10. The length of the fracture is 10 m. The load σ_y applied on the top edge of the block is 5 MPa. The friction coefficient μ_f of the fracture surface is 0.3. The Young's modulus E and the Poisson's ratio ν of the block are 20 GPa and 0.2, respectively. It should be noted that the accuracy of imposing contact constraints in the normal direction depends on the magnitude of penalty parameter k_N ; larger penalty parameter leads to more accurate contact constraints. However, a large penalty parameter will result in an ill-conditioned stiffness matrix and retard the convergence of the iteration. On the other hand, the oscillations in the contact stress fields [63] will intensify as the penalty parameters increase. Hence, some balance must be sought. Therefore, in this paper, both the normal and tangential penalty parameters, k_N and k_T are taken as 10^4 GPa/m [63,64] through trial and numerical experimentation.

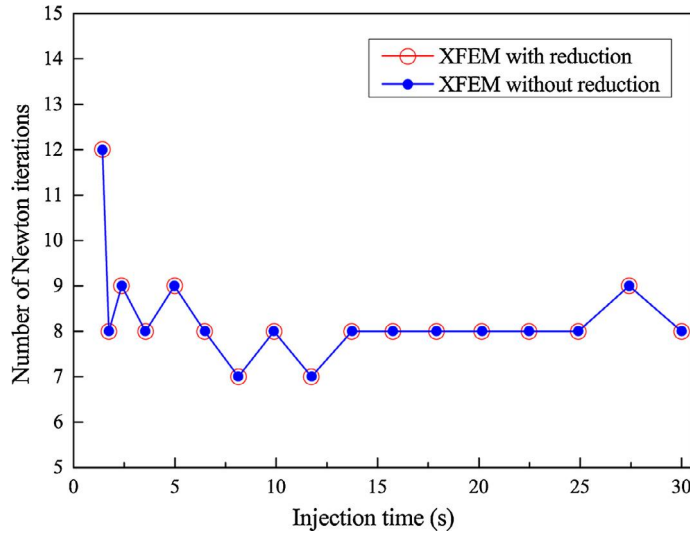


Fig. 8. Number of Newton-Raphson iterations required at different injection time instants.

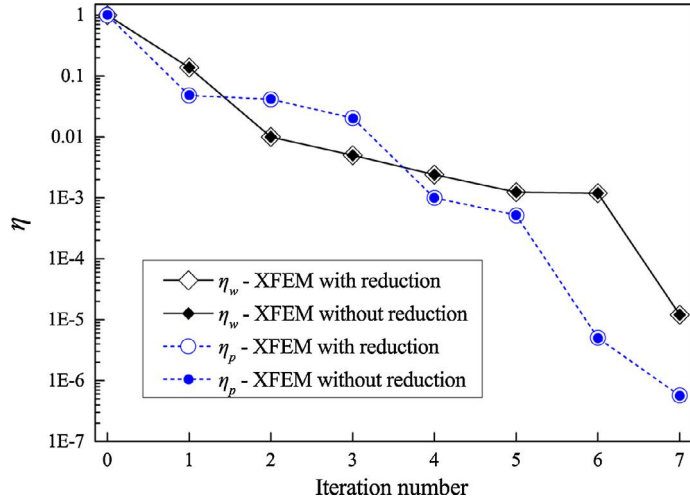


Fig. 9. Convergence curves of nonlinear fluid-solid coupling iterations with and without reduction at the last time step.

The convergence profiles are shown in Fig. 11 from which we can see that the convergence curve of the proposed iteration scheme with reduction technique coincides exactly with that without reduction. For both schemes, the iteration converges after 13 iteration steps when η_c equals $6.4e-11$. The maximum principal stress contours obtained from the XFEM solutions after convergence are plotted in Fig. 12(a and b). In addition, the FEM solution of a model with 6806 elements is presented in Fig. 12(c). In this paper, the positive value of stress indicates tension. It can be seen that the stress distributions for all three cases are almost identical. In order to make a more detailed comparison, the curves of relative sliding (shear displacement) between fracture surfaces along the fracture are plotted in Fig. 13. Good agreements can be observed between the three different numerical schemes. This means that the reduction technique is applicable to the contact iteration in the context of the XFEM. The comparison of the CPU times is given in Fig. 14. It is clearly seen that the reduction technique can greatly reduce the CPU time as in the case of the fluid-solid coupling problem discussed in the previous section. Specifically, as the dimensionality of the linear system to be solved at each iteration step substantially decreases from 4639 (i.e., the number of total DOFs) to 120 (i.e., the number of enriched DOFs), the total CPU time is reduced by 67 percent from 51.4 s to 17.0 s with an acceleration ratio of 3.0. Therefore, we can conclude that the iteration scheme with reduction technique has noticeable acceleration performance without affecting the results, or weakening the robustness and convergence, in comparison with the standard iteration scheme.

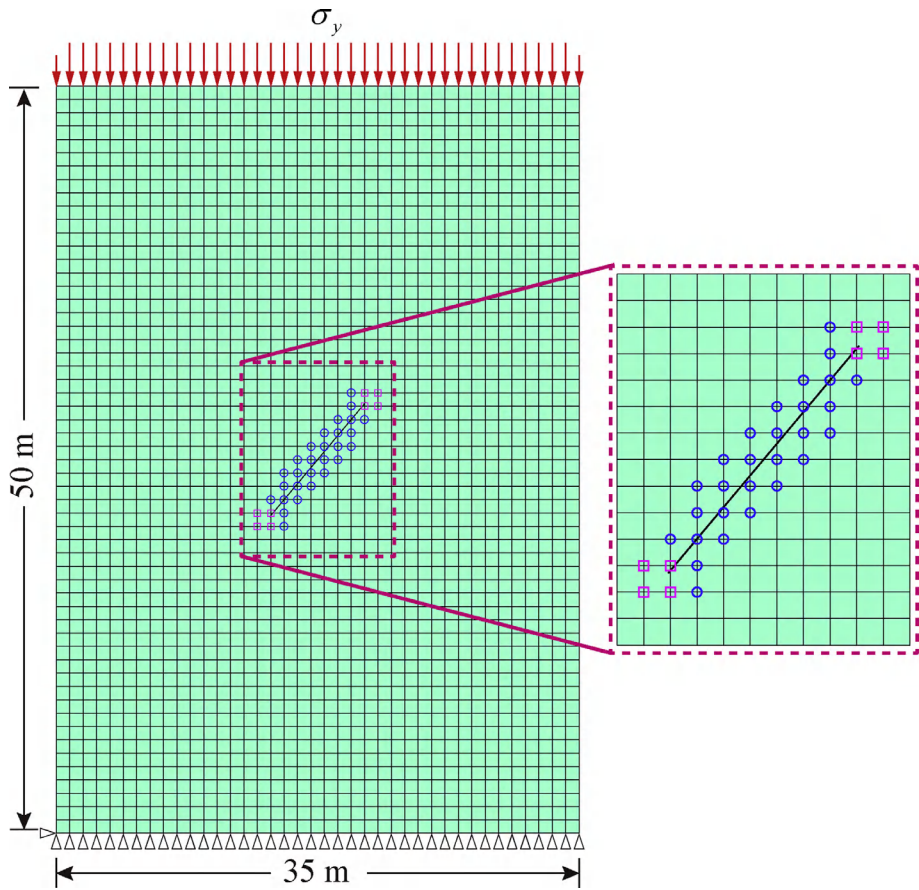


Fig. 10. Finite element model of a plane strain block loaded in compression with a fracture at the angle of 50 degrees relative to the horizontal direction. The model is composed of 2280 standard finite element nodes, 28 Heaviside enriched nodes marked with blue circles and 8 fracture-tip enriched nodes marked with magenta squares. The number of total free DOFs and enriched DOFs equal 4639 and 120, respectively. (For interpretation of the references to color in this figure legend, the reader is referred to the web version of this article.)

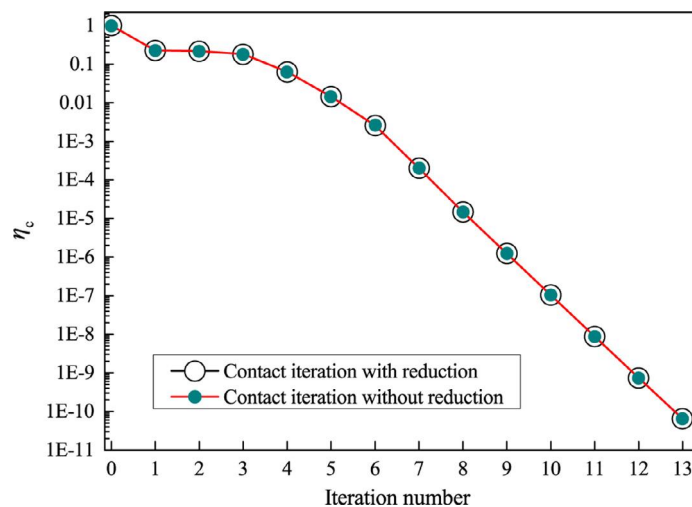


Fig. 11. Convergence curves of contact iterations with and without reduction.

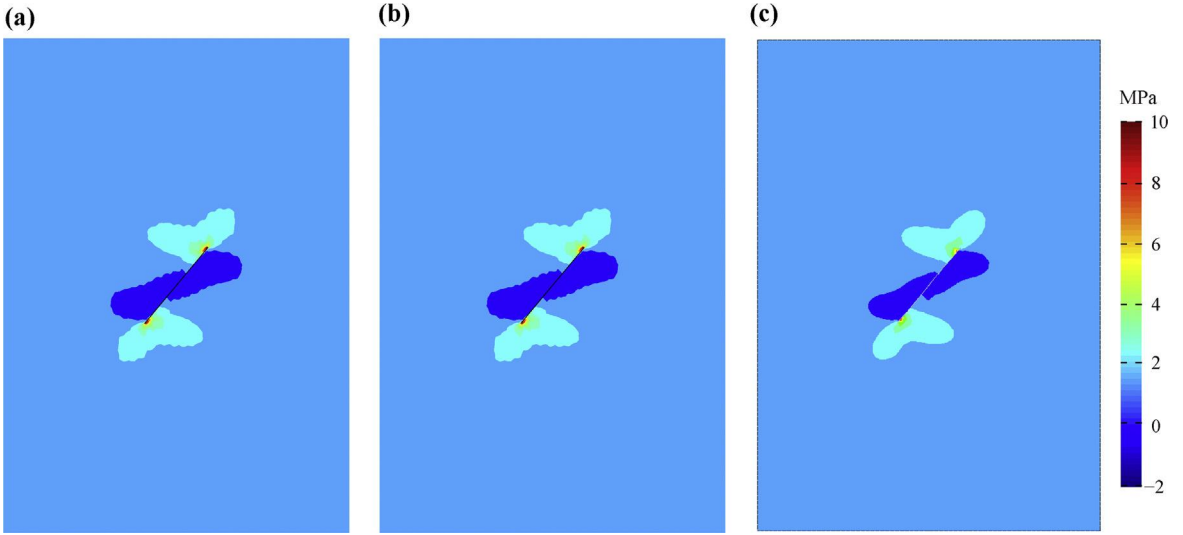


Fig. 12. Contours of maximum principal stress corresponding to (a) XFEM solution with reduction technique, (b) XFEM solution without reduction technique, and (c) FEM solution.

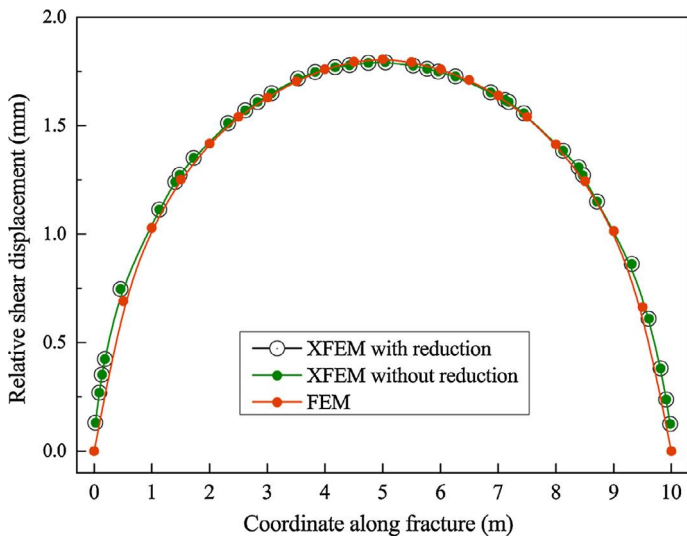


Fig. 13. Comparison of relative sliding (shear displacement) between fracture surfaces.

4.3. Verification of reduction technique for the case where both iterations exist

In this section, we continue to check if the reduction technique has an effect on the results for the case where both the fluid-solid coupling iteration and the contact iteration exist through an example shown in Fig. 15. Additionally, we will also check the treatment method of the conditions of pressure continuity and mass balance at intersection points of hydraulic fractures through this example. The model is assumed to be symmetrical about the central plane and only the right-hand side is considered. Frictional coefficient μ_f of these pre-existing fractures is 0.3. The initial hydro-fracture is positioned on the left edge of the model. The remote in-situ stresses in x and y directions, σ_H and σ_h , are 5 MPa and 4 MPa, respectively. Material properties of the formation and the fracturing parameters are the same as in Table 1. There are a large number of studies reported on the interaction between the hydro-fracture and natural fracture [7,8,12,13,65–68]. In this and the next example, an extended Renshaw and Pollard criterion [69] based on the linear elastic fracture mechanics solution for the stresses is adopted to predict whether a hydro-fracture will propagate across or arrested by the frictional fracture [13,68].

Before performing the simulation, it is still necessary to make some assumptions to achieve a robust numerical model. If the hydro-fracture is arrested by the frictional pre-existing fracture, a T-shaped fracture appears at the intersection point and the fluid is assumed to invade directly into two fracture branches. Then, the hydro-fracture diverts into the pre-existing frac-

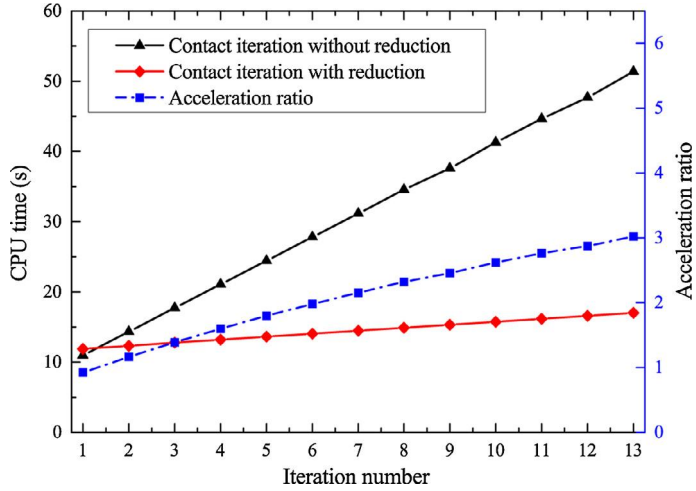


Fig. 14. Comparison of CPU times consumed by XFEM contact iterations with and without reduction technique.

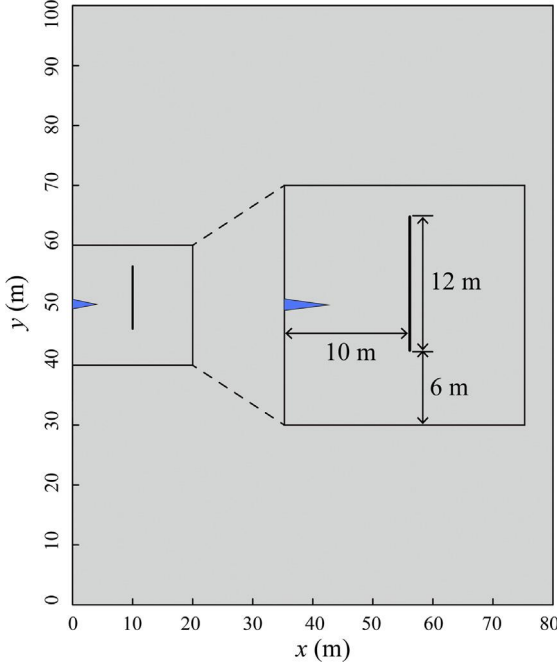


Fig. 15. Illustration of the fracture geometries where the solid line represents pre-existing frictional fracture. The boxed region ($20\text{ m} \times 20\text{ m}$) is meshed into 1600 elements of size $0.5\text{ m} \times 0.5\text{ m}$, and the rest region of the model is meshed into 1312 elements.

ture and propagates along it until reaches the tip of the pre-existing fracture. In other words, growth of the hydraulic fracture in the direction away from the pre-existing fracture is prevented. It is also assumed in this study that after the fluid flows into the frictional fracture, if some part of the frictional fracture is found to be closed (width is less than 0.01 mm), then the fluid nodes will be removed from the closed part.

It is well known that the Newton-Raphson iteration converges to the exact solution rapidly in the first few iteration steps if the initial guess is properly selected [70]. This feature of the Newton-Raphson can also be observed in the convergence curves of the FSC iteration shown in Fig. 9 in which η_w and η_p drop to quite small values, 0.01 and 0.04, respectively, after only two FSC iterations. Therefore, in order to further reduce the calculation amount, we also run the simulation by only performing the contact iteration during the first three FSC iterations within each time step. Then, the contact solution is kept fixed because the slightly changing fluid pressure in the next FSC iterations will not abruptly change the contact solution until the next time step when the fracture network evolves. Finally, it should be noted that the linear elastic fracture mechanics assumption leads to negative net pressure near the fracture tip. Therefore, in this and the next section, the zero

net pressure boundary condition [71,72] is applied at the tip of the hydro-fracture since the length of the zone with negative net pressure is negligible compared to the fracture length.

The fracture opening distributions at different time instants ($t_1 = 28.6$ s, $t_2 = 79.1$ s, and $t_3 = 146.1$ s) are shown in Fig. 16, in which the fracture segments surrounded by the pink boxes are close and in contact. Fig. 16(a) depicts that the surfaces of the pre-existing fracture are in contact. According to the extended Renshaw and Pollard criterion, the hydro-fracture will be arrested, then the hydro-fracture diverts into the frictional fracture and propagates along it in both the upwards and downwards directions, as shown in Fig. 16(b). It can be observed that the surfaces of the top part of the frictional fracture are still in contact under the action of in-situ stress. Afterwards, the propagation paths of the upper and the lower branches are different since the frictional fracture is not symmetrical about the horizontal axis of $y = 50$ m, as depicted in Fig. 16(c).

Furthermore, the distributions of the net fluid pressure inside the frictional fracture at t_2 and t_3 are given in Fig. 17, in which the results obtained without using the reduction technique and the results obtained by performing the contact iteration during only the first three FSC iterations within each time step are also shown. From this figure we observe that the reduction technique has no effect on the simulation results for the case where both hydro-fracture and frictional fracture exist. On the other hand, it can be observed that the treatment method of the contact iteration almost has no effect on the simulation results, indicating that the slightly changing fluid pressure in the fourth and following FSC iterations is not able to change the contact status.

The variations of flow rates with injection time at the intersection point of the hydro-fracture and the frictional fracture are given in Fig. 18. It can be observed that the sum of Q_{up} and Q_{down} exactly equals to Q_{in} . Thus, it can be concluded that the balance of flux into and out of the junction, i.e., $Q_{\text{in}} = Q_{\text{up}} + Q_{\text{down}}$, can be automatically satisfied all the time by sharing a common fluid node at the junction as schematically illustrated in Fig. 3, without invoking any other process [8,12] to determine the flux distribution. Moreover, the pressure at the junction point is undoubtedly the same for all branches, because they share the same fluid node.

4.4. Hydraulic fracture network propagation in a formation containing frictional fractures

In this example, we present a hydraulic fracturing simulation in a formation that contains some specified frictional fractures to comprehensively evaluate the performance of the proposed approach. All parameters are the same as those in Section 4.3 except the configurations of pre-existing fractures, as shown in Fig. 19. Five frictional fractures (denoted by FF for simplicity, and marked as (1) to (5)) with the same length of 5 m. FFs (2), (3), (4), (5) are aligned at an angle of 75° with respect to the negative x -direction, while FF (1) is positioned perpendicularly to the x -direction. The block is discretized into 5180 regular quadrilateral elements in total.

The simulation is performed by applying the reduction technique to both the fluid-solid coupling iteration and contact iteration and proceeds until injection time t reaches 453.5 s. Figs. 20 and 21 show the contours of the maximum principal stress of the whole model and fracture opening distributions within the fracturing zone (i.e., the green region shown in Fig. 19), respectively, at different injection time instants (12.8 s, 137.7 s, 229.0 s and 453.5 s). Clearly, a tensile stress zone around the tip of the initial hydro-fracture, induced by the fluid pressure, can be seen from the stress distribution displayed in Fig. 20(a), in which the initial hydro-fracture propagates before reaching FF (1). In addition, the surfaces of frictional fractures are prevented from interpenetrating when they come into contact. However, no significant stress change can be seen in the vicinity of FFs (2) to (5) because no slip occurs along these fractures under the influence of the specific remote in-situ stresses with a relatively small stress difference of 1 MPa. After the initial hydro-fracture intersects with FF (1), according

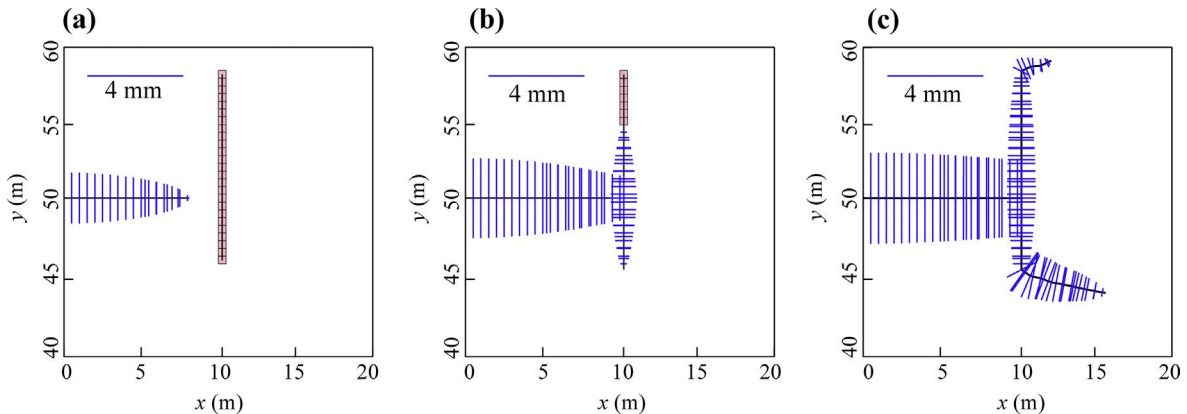


Fig. 16. Fracture opening distributions within the boxed zone shown in Fig. 15 at different injection time instants: (a) $t_1 = 28.6$ s, (b) $t_2 = 79.1$ s, (c) $t_3 = 146.1$ s. The blue bars perpendicular to the fracture segments are proportional in length to the widths of fractures. The fracture segments surrounded by pink boxes are close and in contact. (For interpretation of the references to color in this figure legend, the reader is referred to the web version of this article.)

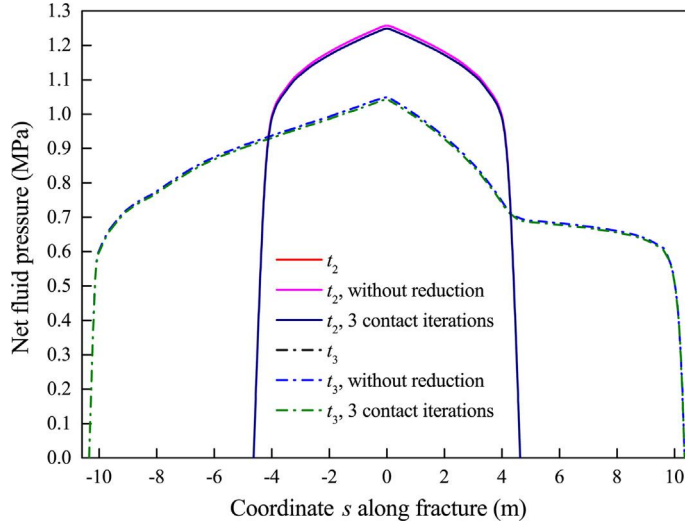


Fig. 17. Net fluid pressure distributions in the vertical fracture shown in Fig. 15 at time instants $t_2 = 79.1$ s and $t_3 = 146.1$ s.

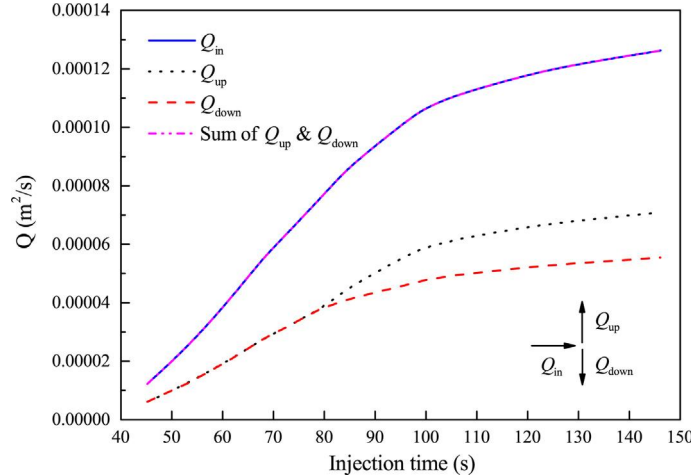


Fig. 18. Evolution of fluid fluxes at the intersection point of the initial hydro-fracture and fractional fracture. Q_{in} denotes the flow from the initial hydro-fracture to the intersection point; Q_{up} denotes the upward flow from the intersection point to the upper half branch, and Q_{down} denotes the downward flow from the intersection point to the lower half branch.

to the extended Renshaw and Pollard criterion no crossing occurs because the coefficient of friction μ_f and the ratio of the remote in-situ stresses σ_H to σ_h are small [68]. Hence, the hydro-fracture propagates along both the upward and downward sides of FF (1), which is presented as a potential flow channel, and keeps propagating until fluid fronts reach the tips of the channel. Afterwards, the two tips of the hydro-fracture synchronously grow and turn to the direction perpendicular to the minimum principal stress, resulting in symmetrical (about the horizontal axis of $y = 50$ m) distributions of propagation paths, as well as stress and fracture opening, as shown in Figs. 20(b) and 21(b). Nonetheless, the symmetry of the propagation paths is broken soon after the oblique FFs (2) and (3) are intersected by the growing hydro-fractures, as can be seen in Figs. 20(c) and 21(c). It is noticed that two branches emerge from both tips of FF (2), while only one from the lower tip of FF (3) and the upper tip stops growing under the combined action of the far-field stresses and the natural-hydraulic fracture interaction. It should be remarked that although FF (2) has two growing branches, the width of the lower one is quite narrow, as can be clearly seen in Fig. 21(c). This evident reduction of fracture width is mainly the result of the stress shadow effect [73], which in this case indicates that the increase of closure stress in its surrounding region induced by the adjacent hydro-fractures above and below it makes it difficult to widen its opening. Thereafter, these three hydraulic fracture tips continue to grow until the lowest one extended from FF (3) meets and intersects with FF (5), leading to a significant tensile stress zone in the vicinity of the newly created intersection point, as shown in Fig. 20(d). It should be noted that the simulation is also run by performing the contact iteration during every FSC iteration within each time step, and the obtained fracture opening

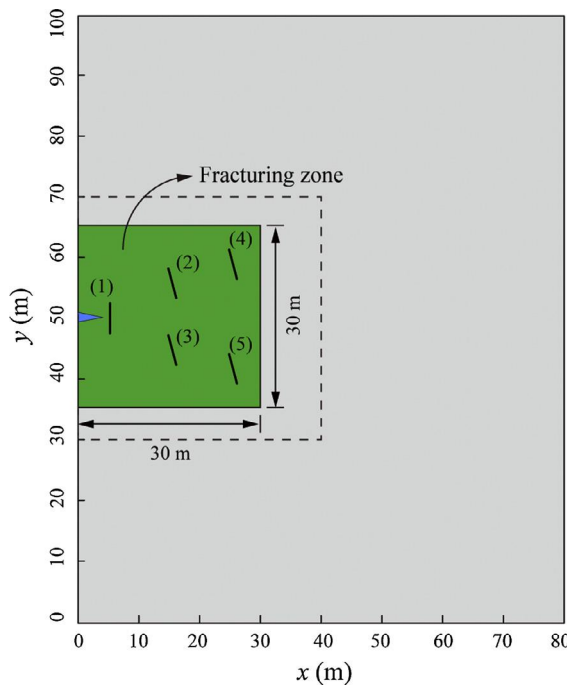


Fig. 19. Illustration of the fracture geometries where the solid lines represent pre-existing frictional fractures marked as (1) to (5). Coordinates of the midpoints of fractures (1) to (5) are (5 m, 50 m), (15 m, 55.5 m), (15 m, 44.5 m), (25 m, 58.5 m) and (25 m, 41.5 m), respectively. The green region (the fracturing zone) is meshed into 3600 elements of size 0.5 m × 0.5 m, and the rest region of the model is meshed into 1580 elements. The dotted-line box is the boundary of a larger fracturing zone with the size of 40 m × 40 m which will be mentioned later in this section. (For interpretation of the references to color in this figure legend, the reader is referred to the web version of this article.)

distributions as well as the contact status are the same. Therefore, it can be concluded that the treating method of the contact iteration performs well and is acceptable for the cases presented in this paper. However, it should also be pointed out that for the extreme cases that involve more fractures, more complex fracture configurations, stronger fracture interactions, more viscous fluid, or dynamic loading condition, the number of contact iterations performed during each time step must be properly chosen through trial and numerical experimentation.

The variations of flow rates with injection time at the intersection point (the junction) of FF (1) are given in Fig. 22. The balance of flux into and out of the junction, i.e., $Q_{in} = Q_{up} + Q_{down}$, is satisfied all the time by sharing a common fluid node at the junction. After the time instant around $t = 140$ s when FFs (2) and (3) are involved in the fracture network, Q_{down} and Q_{up} gradually increases and decreases, respectively, and this variation tendency is in accordance with the fracture opening distributions shown in Fig. 21(c and d), where Q_{down} related fractures have the wider opening than those related to Q_{up} . Meanwhile, as the fracture network evolves, the flux into the junction, Q_{in} , gradually approaches to the total injection rate Q_{inj} , as shown in Fig. 22.

In order to illustrate the performance of the reduction technique, the simulation is carried out for four times in total using four different options of the reduction technique: option (1) reduction technique is applied to both FSC iteration and contact iteration; option (2) applied only to FSC iteration; option (3) applied only to contact iteration, and option (4) no reduction technique is applied. Just as expected, the simulation results, including stress distributions and fracture opening profiles, are completely identical to each other. The consumed CPU times for the above four options and the corresponding acceleration ratios are reported in Figs. 23 and 24, respectively, from which significant performance improvements can be seen. More precisely, in Fig. 23, the final CPU times for options (1) to (4) are 30.7 min, 136.2 min, 96.5 min, and 268.9 min, respectively. The decrease of CPU time from 268.9 min of option (4) to 30.7 min of option (1), with an acceleration ratio up to 8.76, reveals a striking improvement in overall computation efficiency. This improvement is obviously attributed to the considerable decrease of the sizes of linear systems achieved via the application of the reduction technique. Considering the FSC iteration of the last time step for example, as many as 5723 nodes (including 5325 standard nodes, 398 enriched nodes and 293 fluid nodes) are included in the calculation for option (4) and the size of the resulting linear system is $11,739 \times 11,739$. In contrast, only 398 enriched nodes related to the calculation of fracturing widths as well as 293 fluid nodes are included for option (1), leading to a linear system with size 1089×1089 which is considerably smaller than the original size. Nevertheless, the final acceleration ratios for option (2) and option (3) are 1.96 and 2.84, respectively, which are not as significant as option (1), suggesting that the reduction technique should be applied to both the FSC and contact iterations to achieve sufficient performance improvement.

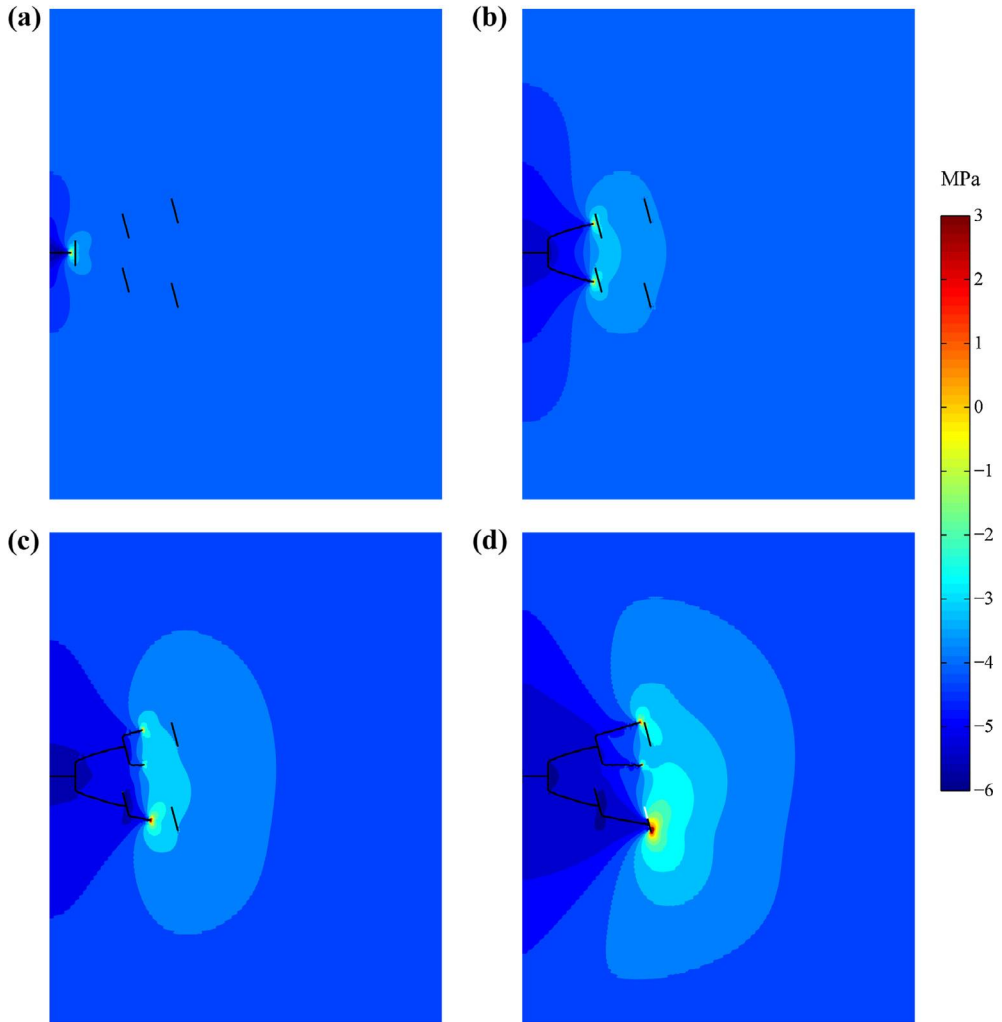


Fig. 20. Contours of the maximum principal stress of the whole model at different injection time instants: (a) $t = 12.8$ s, (b) $t = 137.7$ s, (c) $t = 229.0$ s and (d) $t = 453.5$ s. The solid black lines represent propagation paths.

Finally, in order to investigate the effect of the problem scale on the performance of the reduction technique, the simulation is performed again with a larger fracturing zone of size $40\text{ m} \times 40\text{ m}$, as shown by the dotted-line box in Fig. 19. The fracturing zone is meshed into 6400 elements of size $0.5\text{ m} \times 0.5\text{ m}$, and the rest region of the model contains 1696 elements. Therefore, the number of standard DOFs is increased by 1.6 times from 10,650 to 16,554 compared to the original FEM model in which the fracturing zone contains 3600 elements. The reduction technique is applied to both iterations. It is found that the simulation results including stress distribution and fracture opening are identical to those obtained previously. More importantly, the acceleration effect of the reduction technique becomes more remarkable as the problem scale increases, as shown in Fig. 25. The maximum acceleration ratio is 16.27 and is much bigger than 8.76 of the original smaller model. Therefore, it can be seen that, in general, the larger the problem scale is (usually means more FEM elements), the bigger the acceleration ratio will be.

Compared to our proposed model, some simplifications have to be made in some other numerical methods to reduce the computational cost when dealing with large-scale problems. For example, some key profiles (e.g., stress intensity factors and fracture widths) are determined directly from the analytical solutions [5,13]. However, since the analytical solution is not able to precisely account for the effects of natural fractures and stress shadow, which are critical for the simulation results [74], the numerical accuracy may not be as good as the proposed method. Additionally, uniform fluid pressure along the hydro-fracture is often assumed by researchers to reduce the computation time [14,29,30]. Apparently, this assumption may lead to inaccurate simulation results. In conclusion, after applying the reduction technique, the XFEM-based numerical models are competitive in terms of both computational cost and numerical accuracy.

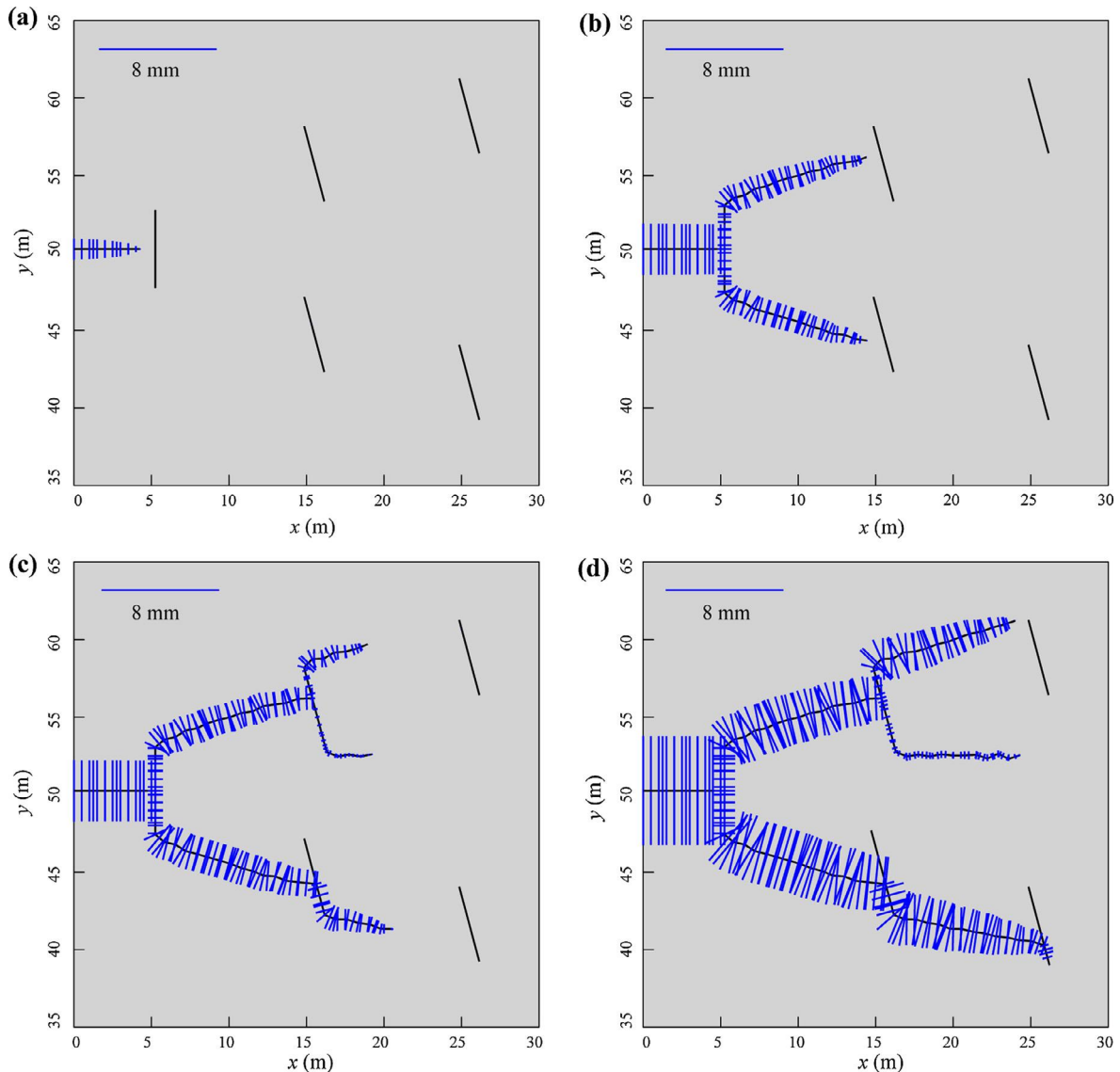


Fig. 21. Fracture opening distributions within the fracturing zone shown in Fig. 19 at different injection time instants: (a) $t = 12.8$ s, (b) $t = 137.7$ s, (c) $t = 229.0$ s and (d) $t = 453.5$ s.

5. Conclusions

The motivation of this work is driven by the requirement to improve the computational efficiency in the modeling of large-scale hydraulic fracturing processes where preexisting frictional fractures are considered. The contribution of the present study lies in the application of the reduction technique to a tightly coupled numerical model to simulate hydraulic fracturing in fractured media within the framework of XFEM. Firstly, the model explicitly incorporates the effect of hydrofractures and natural fractures without requiring the mesh to conform to the fracture geometry. Hence, the challenge of high computational cost induced by the complex meshing is overcome. Secondly, since the fracture widths directly and exclusively depend on the DOFs of enriched nodes, the reduction technique can significantly reduce the sizes of the nonlinear systems by removing the standard DOFs, which have no contribution to fracture opening. After applying the reduction technique to the fluid-solid coupling iteration and the contact iteration, an additional matrix inversion operation of the stiffness matrix is required, but it needs to be performed for only one time right at the beginning of a simulation. In the proposed model, the penalty method within the framework of plasticity theory of friction is used to model the nonlinear frictional contact behavior between frictional fracture faces. The extended Renshaw and Pollard criterion is used to predict whether a

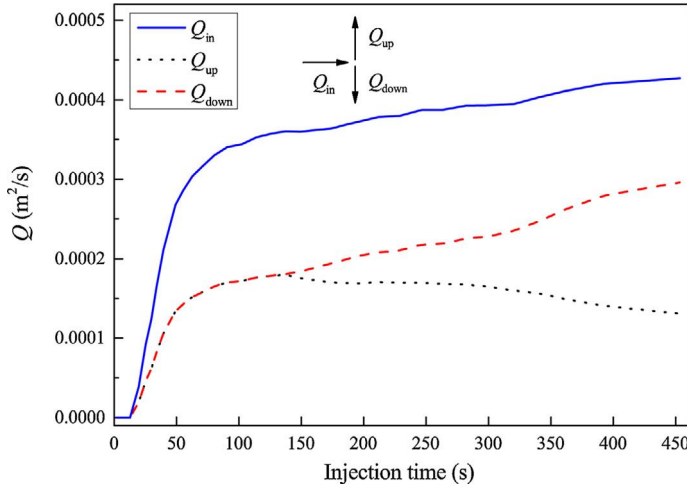


Fig. 22. Evolution of fluid fluxes at the intersection point of the initial hydro-fracture and FF (1). $Q_{in} = Q_{up} + Q_{down}$ holds all the time.

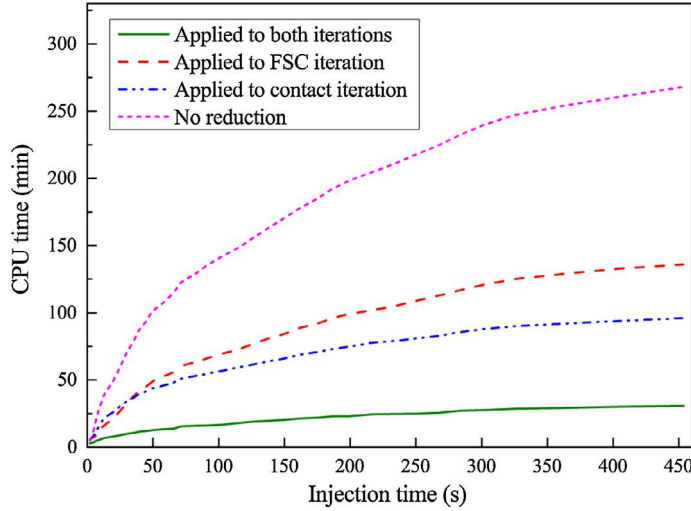


Fig. 23. Consumed CPU times for different application options of the reduction technique at different injection times.

hydro-fracture will propagate across a frictional fracture. The backtracking algorithm is introduced to stabilize the Newton-Raphson iterative procedure which is used to solve the coupled equilibrium and flow continuity equations.

The performance of the established numerical model has been demonstrated through four examples. The first two illustrative examples indicate that the proposed model is accurate, and the reduction technique shows remarkable acceleration effects during the processes of both the fluid-solid coupling iteration and the contact iteration without worsening the convergence or losing the computational accuracy. In the third example, it is shown that the total computational cost can be further reduced without decreasing the accuracy by only performing the contact iteration during the first three FSC iterations within each time step. In addition, the third example also indicates that the mass balance at intersection points of fractures can be automatically satisfied by sharing a common fluid node. This strategy is efficient as it invokes no other procedures to determine the flux distribution at these intersection points. In the last example, the total computational cost is dramatically reduced with an acceleration ratio up to 8.76. However, applying the reduction technique only to the fluid-solid coupling iteration or only to the contact iteration results in much lower acceleration ratios of 1.96 and 2.84, respectively. Consequently, it is strongly suggested that the reduction technique should be applied to both types of iterations to achieve the maximum acceleration effect. In fact, the acceleration ratio is problem dependent and, more importantly, the acceleration effect becomes more remarkable as the problem scale increases.

In conclusion, this study demonstrates that, with the aid of the reduction technique, the XFEM is capable of modeling complex fracture network propagation with dramatically decreased computational cost. On the other hand, as the complicated mechanisms of how hydro-fractures interact with natural fractures, how fluid flow interacts with elastic deformation

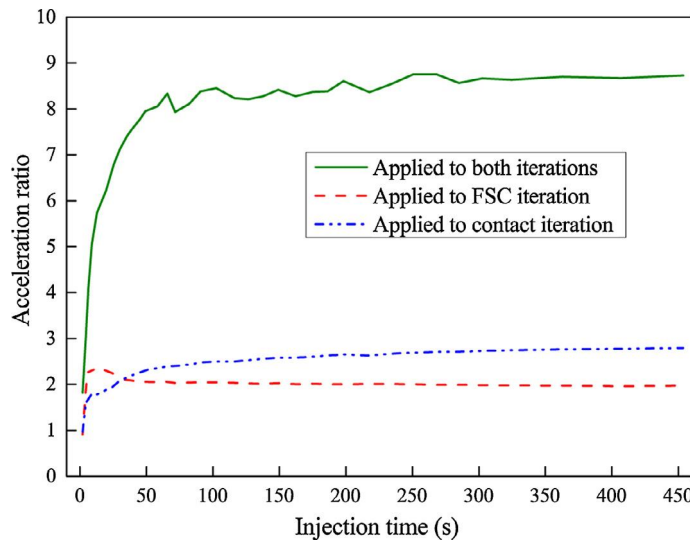


Fig. 24. Evolutions of acceleration ratios with different application options of the reduction technique at different injection times.

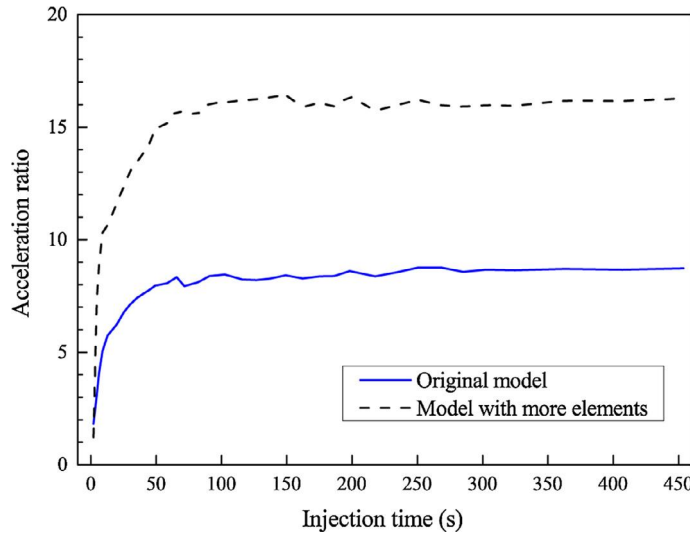


Fig. 25. Comparison of acceleration ratios of the original model and the model with more elements.

of fractures, and how faces of frictional fracture interact with each other are all considered and correctly modeled, the proposed method is able to achieve superior accuracy in comparison to some other numerical methods with various simplifications. The great advantages of XFEM, the high accuracy, as well as the computational efficiency make the proposed numerical method an attractive tool for engineering design of hydraulic fracturing treatments. It is therefore strongly recommended to adopt the reduction technique in the XFEM-based hydraulic fracturing simulators.

Acknowledgements

This work was jointly supported by the National Natural Science Foundation of China (Grant Nos. 11472263 and 11525211) and CNPC-CAS Strategic Cooperation Research Program (Grant No. 2015A-4812).

Appendix A

The Newton-Raphson algorithm is sensitive to the initial guess. If the initial guess is not sufficiently close to the solution, the iterative process may diverge or oscillate between two solutions. This issue is especially remarkable for the Newton-

Raphson procedure of solving the highly nonlinear fluid-solid coupling equations. In contrast, for the Newton-Raphson iteration procedure of solving the contact problem, the zero initial guess of displacement field is generally feasible. In this section, an improvement strategy called the backtracking algorithm [70] is introduced to stabilize the convergence process for the Newton-Raphson iteration procedure of solving the highly nonlinear fluid-solid coupling system. For simplicity, let \mathbf{c}^{new}

and \mathbf{c}^{old} represent $\begin{pmatrix} \mathbf{U}_e \\ \mathbf{P} \end{pmatrix}^{i+1}$ and $\begin{pmatrix} \mathbf{U}_e \\ \mathbf{P} \end{pmatrix}^i$, respectively. Thus, we can define the Newton step $\delta\mathbf{c}$ as follows

$$\delta\mathbf{c} = -\frac{\mathbf{R}_R}{\mathbf{J}_R} \quad (\text{A1})$$

$$\mathbf{c}^{\text{new}} = \mathbf{c}^{\text{old}} + \delta\mathbf{c} \quad (\text{A2})$$

A reasonable approach to deciding whether to accept the Newton step $\delta\mathbf{c}$ or not is to request that the Newton step decreases $|\mathbf{R}_R|^2 = \mathbf{R}_R^T \mathbf{R}_R$ (the superscript is omitted for simplicity), or, in other words, minimizes the following objective function

$$f = \frac{1}{2} \mathbf{R}_R^T \mathbf{R}_R \quad (\text{A3})$$

where $\frac{1}{2}$ is for later convenience. Fortunately, it can be noticed that the Newton step is always the descent direction for f , because

$$\nabla f \delta\mathbf{c} = \left(\mathbf{R}_R^T \mathbf{J}_R \right) \left(-\frac{\mathbf{R}_R}{\mathbf{J}_R} \right) = -\mathbf{R}_R^T \mathbf{R}_R < 0 \quad (\text{A4})$$

Therefore, the strategy is relatively simple: Try a full Newton step first, and if it increases f , then backtrack along the Newton direction until an acceptable step is obtained. As the Newton step is always the decent direction for f , it is guaranteed to find an acceptable step.

A parameter λ is defined to adjust the size of the Newton step

$$\mathbf{c}^{\text{new}} = \mathbf{c}^{\text{old}} + \lambda \delta\mathbf{c} \quad (0 < \lambda \leq 1) \quad (\text{A5})$$

The purpose is to find an acceptable λ that makes $f(\mathbf{c}^{\text{new}})$ decrease sufficiently. The backtracking algorithm [70] can be applied to determine λ . A parameter α is used in the following equation to avoid a too slowly decreasing f

$$f(\mathbf{c}^{\text{new}}) \leq f(\mathbf{c}^{\text{old}}) + \alpha \nabla f \cdot \delta\mathbf{c} \quad (0 < \alpha < 1) \quad (\text{A6})$$

and α is suggested to be 10^{-4} . The backtracking procedure can be implemented as follows.

Define

$$g(\lambda) \equiv f(\mathbf{c}^{\text{old}} + \lambda \delta\mathbf{c}) \quad (\text{A7})$$

so that

$$g'(\lambda) = \nabla f \delta\mathbf{c} \quad (\text{A8})$$

Given a λ , we can get $g(\lambda)$ and $g'(\lambda)$, therefore, for the first backtrack, $g(0)$, $g'(0)$, $g(1)$ and $g'(1)$ are all available. So that $g(\lambda)$ can be approximately written as a quadratic

$$g(\lambda) \approx g(0) + g'(0)\lambda + [g(1) - g(0) - g'(0)]\lambda^2 \quad (\text{A9})$$

The above quadratic has a minimum when

$$\lambda = -\frac{g'(0)}{2[g(1) - g(0) - g'(0)]} \quad (\text{A10})$$

We set $\lambda_{\min} = 0.1$ to avoid a too small λ . Once we get λ_1 of the previous backtrack and λ_2 of the second most recent backtrack, then, for the second and subsequent backtracks, we can approximate $g(\lambda)$ as a cubic

$$g(\lambda) \approx a\lambda^3 + b\lambda^2 + g'(0)\lambda + g(0) \quad (\text{A11})$$

where the coefficients a and b can be calculated by

$$\begin{bmatrix} a \\ b \end{bmatrix} = \frac{1}{\lambda_1 - \lambda_2} \begin{bmatrix} 1/\lambda_1^2 & -1/\lambda_2^2 \\ -\lambda_2/\lambda_1^2 & \lambda_1/\lambda_2^2 \end{bmatrix} \begin{bmatrix} g(\lambda_1) - g'(0)\lambda_1 - g(0) \\ g(\lambda_2) - g'(0)\lambda_2 - g(0) \end{bmatrix} \quad (\text{A12})$$

The minimum of the above cubic is at

$$\lambda = \frac{-b + \sqrt{b^2 - 3ag'(0)}}{3a} \quad (\text{A13})$$

It is enforced that λ lies between $\lambda_{\max} = 0.5\lambda_1$ and $\lambda_{\min} = 0.1\lambda_1$.

References

- [1] Economides MJ, Martin T. Modern fracturing enhancing natural gas production. Houston (TX): BJ Services Company; 2007.
- [2] Laguna Wd. Disposal of radioactive wastes by hydraulic fracturing: Part I. General concept and first field experiments. *Nucl Eng Des* 1966;3:338–52.
- [3] Legarth B, Huenges E, Zimmermann G. Hydraulic fracturing in a sedimentary geothermal reservoir: results and implications. *Int J Rock Mech Min Sci* 2005;42:1028–41.
- [4] Rutqvist J, Tsang CF. A study of caprock hydromechanical changes associated with CO₂-injection into a brine formation. *Environ Geol* 2002;42:296–305.
- [5] Weng X. Modeling of complex hydraulic fractures in naturally fractured formation. *J Unconv Oil Gas Resour* 2015;9:114–35.
- [6] Kresse O, Weng X, Gu H, Ruiting W. Numerical modeling of hydraulic fractures interaction in complex naturally fractured formations. *Rock Mech Rock Eng* 2013;46:555–68.
- [7] Dahi-Taleghani A, Olson JE. Numerical modeling of multistranded-hydraulic-fracture propagation: accounting for the interaction between induced and natural fractures. *SPE J* 2011;16:575–81.
- [8] Zhang X, Jeffrey RG. The role of friction and secondary flaws on deflection and re-initiation of hydraulic fractures at orthogonal pre-existing fractures. *Geophys J Int* 2006;166:1454–65.
- [9] Seseaty V, Ghassemi A. A numerical study of sequential and simultaneous hydraulic fracturing in single and multi-lateral horizontal wells. *J Pet Sci Eng* 2015;132:65–76.
- [10] Carrier B, Granet S. Numerical modeling of hydraulic fracture problem in permeable medium using cohesive zone model. *Eng Fract Mech* 2012;79:312–28.
- [11] McClure MW, Horne RH. Discrete fracture network modeling of hydraulic stimulation: coupling flow and geomechanics. Berlin: Springer; 2013.
- [12] Zhang X, Jeffrey RG. Role of overpressurized fluid and fluid-driven fractures in forming fracture networks. *J Geochem Explor* 2014;144:194–207.
- [13] Weng X, Kresse O, Cohen C-E, Wu R, Gu H. Modeling of hydraulic-fracture-network propagation in a naturally fractured formation. *SPE Prod Oper* 2011;26:368–80.
- [14] Olson JE, Taleghani AD. Modeling simultaneous growth of multiple hydraulic fractures and their interaction with natural fractures. In: SPE hydraulic fracturing technology conference. The Woodlands (TX): Society of Petroleum Engineers; 2009.
- [15] Nagel NB, Gil I, Sanchez-nagel M, Damjanac B. Simulating hydraulic fracturing in real fractured rock-overcoming the limits of pseudo 3D models. In: SPE hydraulic fracturing technology conference. The Woodlands (TX): Society of Petroleum Engineers; 2011.
- [16] Nagel NB, Sanchez MA, Lee B. Gas shale hydraulic fracturing: a numerical evaluation of the effect of geomechanical parameters. In: SPE hydraulic fracturing technology conference. The Woodlands (TX): Society of Petroleum Engineers; 2012.
- [17] Shimizu H, Muratab S, Ishidab T. The distinct element analysis for hydraulic fracturing in hard rock considering fluid viscosity and particle size distribution. *Int J Rock Mech Min Sci* 2011;48:712–27.
- [18] Papanastasiou P. An efficient algorithm for propagating fluid-driven fractures. *Comput Mech* 1999;24:258–67.
- [19] Chen Z. Finite element modelling of viscosity-dominated hydraulic fractures. *J Pet Sci Eng* 2012;88–89:136–44.
- [20] Wangen M. Finite element modeling of hydraulic fracturing on a reservoir scale in 2D. *J Pet Sci Eng* 2011;77:274–85.
- [21] Guo T, Zhang S, Zou Y, Xiao B. Numerical simulation of hydraulic fracture propagation in shale gas reservoir. *J Nat Gas Sci Eng* 2015;26:847–56.
- [22] Bao JQ, Fathi E, Ameri S. A coupled finite element method for the numerical simulation of hydraulic fracturing with a condensation technique. *Eng Fract Mech* 2014;131:269–81.
- [23] Lecampion B. An extended finite element method for hydraulic fracture problems. *Commun Numer Methods Eng* 2009;25:121–33.
- [24] Mohammadnejad T, Khoei AR. An extended finite element method for hydraulic fracture propagation in deformable porous media with the cohesive crack model. *Finite Elem Anal Des* 2013;73:77–95.
- [25] Gordeliy E, Peirce A. Coupling schemes for modeling hydraulic fracture propagation using the XFEM. *Comput Methods Appl Mech Eng* 2013;253:305–22.
- [26] Khoei AR, Hirmand M, Vahab M, Bazargan M. An enriched FEM technique for modeling hydraulically driven cohesive fracture propagation in impermeable media with frictional natural faults: numerical and experimental investigations. *Int J Numer Methods Eng* 2015;104:439–68.
- [27] Wang HY. Numerical investigation of fracture spacing and sequencing effects on multiple hydraulic fracture interference and coalescence in brittle and ductile reservoir rocks. *Eng Fract Mech* 2016;157:107–24.
- [28] Réthoré J, Borst R, Abellan M. A two-scale approach for fluid flow in fractured porous media. *Int J Numer Methods Eng* 2007;71:780–800.
- [29] Khoei AR, Vahab M, Hirmand M. Modeling the interaction between fluid-driven fracture and natural fault using an enriched-FEM technique. *Int J Fract* 2016;197:1–24.
- [30] Taleghani AD, Olson JE. How natural fractures could affect hydraulic-fracture geometry. *SPE J* 2014;19:161–71.
- [31] Shi F, Wang X, Liu C, Liu H, Wu H. A coupled extended finite element approach for modeling hydraulic fracturing in consideration of proppant. *J Nat Gas Sci Eng* 2016;33:885–97.
- [32] Wrobel LC, Aliabadi MH. The boundary element method. New York: John Wiley & Sons; 2002.
- [33] Boukouvala F, Gao Y, Muzzio F, Ierapetritou MG. Reduced-order discrete element method modeling. *Chem Eng Sci* 2013;95:12–26.
- [34] Zienkiewicz OC, Taylor RL, Zhu JZ. The finite element method: its basis and fundamentals. 7th ed. Oxford (UK): Butterworth-Heinemann; 2013.
- [35] Moës N, Dolbow J, Belytschko T. A finite element method for crack growth without remeshing. *Int J Numer Methods Eng* 1999;46:131–50.
- [36] Stolarska M, Chopp DL, Moës N, Belytschko T. Modelling crack growth by level sets in the extended finite element method. *Int J Numer Methods Eng* 2001;51:943–60.
- [37] Daux C, Moës N, Dolbow J, Sukumar N, Belytschko T. Arbitrary branched and intersecting cracks with the extended finite element method. *Int J Numer Methods Eng* 2000;48:1741–60.
- [38] Sukumar N, Prevost JH. Modeling quasi-static crack growth with the extended finite element method Part I: computer implementation. *Int J Solids Struct* 2003;40:7513–37.
- [39] Belytschko T, Black T. Elastic crack growth in finite elements with minimal remeshing. *Int J Numer Methods Eng* 1999;45:601–20.
- [40] Budyn É, Zi G, Moës N, Belytschko T. A method for multiple crack growth in brittle materials without remeshing. *Int J Numer Methods Eng* 2004;61:1741–70.
- [41] Mohammadnejad T, Khoei AR. Hydro-mechanical modeling of cohesive crack propagation in multiphase porous media using the extended finite element method. *Int J Numer Anal Methods Geomech* 2013;37:1247–79.
- [42] Khoei AR, Vahab M, Haghigheh E, Moallemi S. A mesh-independent finite element formulation for modeling crack growth in saturated porous media based on an enriched-FEM technique. *Int J Fract* 2014;188:79–108.
- [43] Khoei AR, Hosseini N, Mohammadnejad T. Numerical modeling of two-phase fluid flow in deformable fractured porous media using the extended finite element method and an carelessness equivalent continuum model. *Adv Water Res* 2016;94:510–28.
- [44] Adachi J, Siebrits E, Peirce A, Desroches J. Computer simulation of hydraulic fractures. *Int J Rock Mech Min Sci* 2007;44:739–57.
- [45] Golub GH, Loan CFV. Matrix computations. 3rd ed. Baltimore (MD): Johns Hopkins University Press; 1996.
- [46] Guyan RJ. Reduction of stiffness and mass matrices. *AIAA J* 1965;3:380.
- [47] Kim JG, Boo SH, Lee CO, Lee PS. On the computational efficiency of the error estimator for Guyan reduction. *Comput Methods Appl Mech Eng* 2016;305:759–76.

- [48] Wang Y, Palacios R, Wynn A. A method for normal-mode-based model reduction in nonlinear dynamics of slender structures. *Comput Struct* 2015;159:26–40.
- [49] Noor AK, Peters JM. Reduction technique for tire contact problems. *Comput Struct* 1996;60:223–33.
- [50] Erdogan F, Sih GC. On the crack extension in plates under plane loading and transverse shear. *J Basic Eng-Trans ASME* 1963;85:519–25.
- [51] Moran B, Shih CF. Crack tip and associated domain integrals from momentum and energy balance. *Eng Fract Mech* 1987;27:615–42.
- [52] Batchelor GK. An introduction to fluid dynamics. Cambridge: Cambridge University Press; 1967.
- [53] Khoei AR, Nikbakht M. An enriched finite element algorithm for numerical computation of contact friction problems. *Int J Mech Sci* 2007;49:183–99.
- [54] Gale JFW, Reed RM, Holder J. Natural fractures in the Barnett Shale and their importance for hydraulic fracture treatments. *AAPG Bull* 2007;91:603–22.
- [55] Khoei AR, Vahab M. A numerical contact algorithm in saturated porous media with the extended finite element method. *Comput Mech* 2014;54:1089–110.
- [56] Elguedj T, Gravouil A, Combescure A. A mixed augmented Lagrangian-extended finite element method for modelling elastic-plastic fatigue crack growth with unilateral contact. *Int J Numer Methods Eng* 2007;71:1569–97.
- [57] Khoei AR. Extended finite element method: theory and applications. London: John Wiley & Sons; 2014.
- [58] de Souza Neto EA, Peric D, Owen DRJ. Computational methods for plasticity: theory and applications. New York: John Wiley & Sons; 2011.
- [59] Chen Z, Dongarra J, Luszczek P, Roche K. Self-adapting software for numerical linear algebra and LAPACK for clusters. *Parallel Comput* 2003;29:1723–43.
- [60] Detournay E. Propagation regimes of fluid-driven fractures in impermeable rocks. *Int J Geomech* 2004;4:35–45.
- [61] Hu J, Garagash DI. Plane-strain propagation of a fluid-driven crack in a permeable rock with fracture toughness. *J Eng Mech* 2010;136:1152–66.
- [62] Bunger A, Garagash D, Peirce A. Numerical simulation of hydraulic fracturing in the viscosity dominated regime. In: SPE hydraulic fracturing technology conference. College Station (TX, USA): Society of Petroleum Engineers; 2007.
- [63] Liu F, Borja RI. Stabilized low-order finite elements for frictional contact with the extended finite element method. *Comput Methods Appl Mech Eng* 2010;199:2456–71.
- [64] Liu F, Borja RI. A contact algorithm for frictional crack propagation with the extended finite element method. *Int J Numer Methods Eng* 2008;76:1489–512.
- [65] Warpinski NR, Teufel LW. Influence of geologic discontinuities on hydraulic fracture propagation. *J Petrol Technol* 1987;39:209–20.
- [66] Akulich AV, Zvyagin AV. Interaction between hydraulic and natural fractures. *Fluid Dyn* 2008;43:428–35.
- [67] Zhang Z, Ghassemi A. Simulation of hydraulic fracture propagation near a natural fracture using virtual multidimensional internal bonds. *Int J Numer Anal Methods Geomech* 2010;35:480–95.
- [68] Gu H, Weng X. Criterion for fractures crossing frictional interfaces at non-orthogonal angles. In: 44th US rock symposium, Salt Lake City, Utah; 2010.
- [69] Renshaw CE, Pollard DD. An experimentally verified criterion for propagation across unbounded frictional interfaces in brittle, linear elastic materials. *Int J Rock Mech Min Sci Geomech Abstr* 1995;32:237–49.
- [70] Press W, Teukolsky S, Vetterling W, Flannery B. Numerical recipes in Fortran: the art of scientific computing. New York: Cambridge University Press; 1992.
- [71] Yew CH, Liu GF. The fracture tip and critical stress intensity factor of a hydraulically induced fracture. *SPE Prod Facil* 1993;8:171–7.
- [72] Taleghani AD, Olson JE. Analysis of multistranded hydraulic fracture propagation: an improved model for the interaction between induced and natural fractures. In: SPE annual technical conference and exhibition. New Orleans (LA): Society of Petroleum Engineers; 2009.
- [73] Yew CH, Weng X. Mechanics of Hydraulic Fracturing. 2nd ed. Houston (TX): Gulf Professional Publishing; 2014.
- [74] Wang H, Liu Z, Xu D, Zeng Q, Zhuang Z. Extended finite element method analysis for shielding and amplification effect of a main crack interacted with a group of nearby parallel microcracks. *Int J Damage Mech* 2016;25:4–25.